Single-cell profiling reveals the intratumor heterogeneity and immunosuppressive microenvironment in cervical adenocarcinoma

Yang Peng[1], Yilin Li[2], Jixing Ao[3], Jia Shen[4, 5, 6], Xiang He[4, 5, 6], Dihong Tang[1], Chaonan Chu[1], Congrong Liu[7, #], Liang Weng[4, 5, 6, #]

[1] Fourth Department of Gynecologic Oncology, Hunan Cancer Hospital/The Affiliated Cancer Hospital of Xiangya School of Medicine, Central South University, 283 Tongzipo Road, Changsha 410013, Hunan, China

[2] Department of Pathology, Hunan Cancer Hospital/The Affiliated Cancer Hospital of Xiangya School of Medicine, Central South University, 283 Tongzipo Road, Changsha 410013, Hunan, China

[3] Department of Gynecologic Oncology, Changsha Kexin Cancer Hospital, 292 Fenglinsan Road, Changsha 410004, Hunan, China

[4] Xiangya Cancer Center, Xiangya Hospital, Central South University, Changsha 410008, China

[5] Key Laboratory of Molecular Radiation Oncology of Hunan Province, Changsha 410008, China

[6] Hunan International Science and Technology Collaboration Base of Precision Medicine for Cancer, Changsha 410008, China

[7] Department of Pathology, Third Hospital, School of Basic Medical Sciences, Peking University Health Science Center, Beijing, 100191, China.

[#] Corresponding to: wengliang@csu.edu.cn (L. W.), congrong_liu@hsc.pku.edu.cn (C. L.)

Abstract

Background: Cervical adenocarcinoma (ADC) is more aggressive compared to other types of cervical cancer (CC), such as squamous cell carcinoma (SCC). The tumor immune microenvironment (TIME) and tumor heterogeneity are recognized as pivotal factors in cancer progression and therapy. However, the disparities in TIME and heterogeneity between ADC and SCC are poorly understood.

Methods: We performed single-cell RNA sequencing on 11 samples of ADC tumor tissues, with other 4 SCC samples served as controls. The immunochemistry and multiplexed immunofluorescence were conducted to validate our findings.

Results: Compared to SCC, ADC exhibited unique enrichments in several sub-clusters of epithelial cells with elevated stemness and hyper-malignant features, including the Epi_10_CYSTM1 cluster. ADC displayed a highly immunosuppressive environment characterized by the enrichment of regulatory T cells (Tregs) and tumor-promoting neutrophils. The Epi_10_CYSTM1 cluster recruits Tregs via ALCAM-CD6 signaling, while Tregs reciprocally induce stemness in the Epi_10_CYSTM1 cluster through TGFβ signaling. Importantly, our study revealed that the Epi_10_CYSTM1 cluster could serve as a valuable predictor of lymph node metastasis for CC patients.

Conclusions: This study highlights the significance of ADC-specific cell clusters in establishing a highly immunosuppressive microenvironment, ultimately contributing to the heightened aggressiveness and poorer prognosis of ADC compared to SCC.

Introduction

Cervical cancer (CC) is the fourth leading cause of cancer-related death among all types of women malignancies (Sung et al., 2021). The two major histological types of CC are squamous cell carcinoma of cervix (SCC) and adenocarcinoma of cervix (ADC), accounting for 70% and 25% of all cases, respectively (Cohen, Jhingran, Oaknin, & Denny, 2019). ADC patients tend to have a higher rate of rapid progression, relapse and insensitivity to chemotherapy, radiotherapy and even immunotherapy, making it a more aggressive phenotype than SCC (Sasieni, Castanon, & Cuzick, 2009). Unfortunately, the reasons are not yet well understood due to its rarity. Furthermore, the standard treatment for both types of CC is not stratified based on pathologic types, which can result in treatment failures of ADC patients. Therefore, there is an urgent need for a comprehensive understanding of ADC.

In 2022, the National Comprehensive Cancer Network (NCCN) guidelines recommended pembrolizumab (Keytruda ®, a PD1 blockade) as the first-line combination therapy for late-stage, recurrent and metastatic CC patients with positive PD-L1 expressions (Colombo et al., 2021). It is a milestone that immunotherapy has been updated as a first-line treatment for CC. While it has been reported that 30%-50% of CC patients exhibit positive PD-L1 expression, however, only an estimated 20%-30% are expected to respond positively to PD-1/PD-L1 blockade therapy (Omenai, Ajani, & Okolo, 2022; Sun et al., 2020). Therefore, CC is characterized as an immunosuppressive cancer type, due to modulation of the tumor immune microenvironment (TIME) (Cao et al., 2023). TIME, consisting of tumor cells, immune cells, cytokines and their interactions, predominantly determines the efficacy of immunotherapy (Lv et al., 2022). The mechanisms of tumor immune evasion within the TIME are similar across different types of cancer, involving the deactivation of immune surveillance pathways or recruitment of immunorepressive cells (Vinay et al., 2015). However, the specific characteristics of the TIME in ADC, which is known as insensitive to immunotherapy, remain poorly understood.

Persistent infection with human papillomavirus (HPV) is the primary cause of CC (Mann, Singh, & Kumar, 2023). Approximately 85% of CC patients are identified with HPV infection, while 5%-15% of patients test negative for HPV (X. Yang et al., 2023). It is reported that HPV-negative patients tend to experience worse clinical outcomes, including rapid metastasis to distant organs, and an increased susceptibility to developing resistance to immunotherapy (Fernandes, Viveros-Carreño, Hoegl, Ávila, & Pareja, 2022). However, current therapeutic strategies for CC do not take into account the HPV infection status as a stratification factor. Therefore, it is imperative to investigate the precise mechanisms underlying the development of HPV-negatively infected tumors. In addition, an important and unavoidable clinical issue in CC treatment is post-surgical upstaging, which affects the disease outcome and treatment approach.

To extensively investigate the cellular and molecular heterogeneity of CC, particularly ADC, the utilization of single-cell RNA sequencing (scRNA-seq) technique is crucially needed. In the current study, we focused on the remodeling of TIME in ADC and performed scRNA-seq analysis on 11 ADC samples, with another 4 SCC samples included as controls. By high-throughput analysis, we are able to characterize the landscape of TIME in ADC, with different types of tumor-promoting cells being recruited in the vicinity of the tumor, thus creating an immunosuppressive environment in ADC. The cellular crosstalk analysis provides valuable insights into the interactions between different cell types within the TIME. Furthermore, we have conducted a screening of novel signature genes as prognostic biomarkers for ADC. These biomarkers have the potential to accurately predict lymph node metastasis and may guide personalized treatment decisions more effectively.

Methods

Clinical sample collection

The 15 cases of fresh cervical cancer tissues were collected from Hunan Cancer

Hospital, with informed consent obtained from 15 independent patients. The inclusion criteria are as follows: 1) The diagnosis of CC, with pathological type of ADC or SCC, should be confirmed by pathologists; 2) Pre-surgical FIGO stages should be within the range from IB (which means the tumor mass should be detectable via CT or MRI) to IIA (which means no parametrial involvement, nor distant metastasis), in which patients have explicit indication for radical surgery following NCCN guidelines; 3) No neo-adjuvant treatments should be given before the surgery, including chemotherapy and radiotherapy; 4) The surgery options should be type-C radical hysterectomy and include pelvic lymphadenectomy with/ without para-aortic lymphadenectomy. Detailed information of the 15 patients was listed in **Supplementary Table 1**. This study was supervised and approved by the Ethics Committee Board of Hunan Cancer Hospital.

Sample preparation for single-cell isolation

Immediately after surgical removal, the fresh tumor tissues were washed by saline for 3 times and stored in cold storage solution (MACS® Tissue Storage Solution) for transportation. To prepare high-quality samples, the tissues were cut into pieces to $1mm^3$ and were incubated at 37°C for 30 minutes. 0.25% trypsin solution was used to digest the tissue pieces at 37°C for 10 minutes. Then single-cell samples were filtered through a 70-μm meshed filter and suspended in a red blood cell lysis buffer (MACS® Red Blood Cell Lysis Solution) for dissolution. Before instrumental sequencing, suspension of single cells were visualizing by TC20™ Automated Cell Counter to assess the cell viability. Each sample was confirmed to have a cell viability rate of over 80%.

Single-cell RNA sequencing

The suspension of single cells was transferred onto the 10X Chromium Single-Cell instrument to generate single-cell beads in the emulsion (GEMs). Then the

scRNA-seq libraries were constructed by using the Chromium Next GEM Single Cell 3' Reagent Kits v3 (10X Genomics, USA) and sequenced by using the sequencer Novaseq6000 (Illumina, USA). All procedures were following the manufacturer's protocol.

Dimension reduction and cell clustering

The gene expression matrixes were generated via the Cell Ranger toolkit (version 5.0.0) of 10X Genomics platform. The package of Seurat (version 4.0.5 R) was used to normalize, convert and format data. With the function of RunPCA, the principal component analysis (PCA) was used for data dimension reduction. The functions of FindNeighbors and FindClusters were used for cell clustering. For visualization, the RunUMAP function was performed. In each unsupervised cell cluster, the gene markers were identified by the function of FindAllMarkers with comparison to other clusters. For data processing, cells with low qualities, which showed <200 expressed genes or >25% mitochondrial UMIs (unique molecular identifiers), were excluded.

Cell type annotation

The cell typing was conducted and annotated according to the selected gene markers via CellMarker database and publications (C. Li et al., 2022; Qiu et al., 2023; Xue et al., 2022). The expression of differential expressed genes (DEGs) was used to determine each cell type following the rules: Log_2Foldchange should be > 0.2 and adjusted-*P* values should be < 0.05.

Pseudotime trajectory analysis

To identify the developmental changes of epithelial cells, the pseudotime trajectory analyses were performed by using Monocle2 R package (version 2.22.0), in which Seurat was used as input. Calculated by the Monocle algorithm, the top 50-1000 genes were conducted for differential GeneTest. Then, the DDR-Tree and default

parameters were generated to visualize the translational relationship and developmental orders among different epithelial sub-clusters.

Cell malignancy scoring

Among these epithelial cells, the malignant score of each single cell was predicted by using scCancer R package (Guo et al., 2021). The malignant cells were distinguished from non-malignant cells by inferring large-scale copy-number variations (CNVs), which was calculated by the interCNV R package as described (Guo et al., 2021; Xue et al., 2022).

Signaling pathway enrichment analysis

The biological signaling pathway of each cell cluster was identified by performing Gene Ontology (GO) analyses and Hallmark Pathway enrichment analyses, according to the Molecular Signature Database (MSigDB version 7.5.1). Then DEGs of each cell cluster were converted to ClusterProfiler (version 4.2.2) package for analysis of predicted functions.

CytoTRACE

In order to predict the differential state of cells, scRNA-seq derived data were pass to the CytoTRACE software (version 0.3.3) with R package for further analyses.

Survival analysis

The CESC dataset from TCGA database was downloaded from Xena, with clinical characteristics, survival endpoints and treatments were included. The Kaplan-Meier survival curves were generated by using R software.

Cellular communication analysis

The possible interactions, with ligand-to-receptor communicating signaling pathway,

between two types of cells were analyzed using the R packages of CellChat (version 1.5.0). Seurat was used for normalization and the rank with significance was calculated. The probability of ligand-to-receptor interaction in each signaling pathway was plotted by *P*-value and intensity.

Immunohistochemistry (IHC)

The paraffin-embedded ADC samples (whether post-surgical or biopsy samples) were sectioned into 4μm slides. The protocol of IHC strictly followed our previous published works (Peng et al., 2019). The primary antibody of SLC26A3 was purchased from Santa Cruz Biotechnology (Cat# sc-376187) and diluted at the ratio of 1:20. The protein expression of SLC26A3 was determined using the method of *H*-scoring: *H*-score = intensity score × percentage of positivity. The intensity was scored as: Negative=0, Weak=1, Moderate=2, Strong=3. Samples were grouped as the higher expression group (H-score ≥ 150) and the lower expression (H-score < 150) group of SLC26A3.

Multiplexed immunofluorescence (multi-IF)

The multi-IF was performed using the Opal 6-Plex Manual Detection Kit (NEL811001KT, Akoya), following the manufacturer's instructions. Generally, the slides were stained with each primary antibody sequentially following the staining cycle as: (1) antigen retrieval by citrate (pH=6) at water bath for 30 minutes; (2) independent primary antibody incubation at 4°C atmosphere overnight or 37°C atmosphere for 1 hour; (3) common HRP-crosslinked secondary antibody incubation at 37°C atmosphere for 30 minutes; (4) independent opal reactive fluorophore solution at intended wavelength (opal 570 was excluded in order to save for FOXP3 signal). Each independent primary antibody started a new cycle. After cycles finished, the slides were prepared for incubation of FOXP3 monoclonal antibody with eFluor™ 570 (Thermo Fisher, Cat#41-4777-82) conjugated, as well as DAPI (Sigma) for

nucleus staining.

Statistics

Specific analyses of scRNA-seq data were decoded and visualized by using the R software. Statistics were processed using IBM-SPSS Statistics 20.0 software and R software as well, including Student's *t*-test, two-sided Wilcoxon test, etc. Correlations analysis was performed by the *Chi*-square test. Survival analysis was performed by the Kaplan-Meier method. P values < 0.05 were considered as statistically significant.

Results

Single-cell transcriptomic landscape of cervical cancer

We collected 15 samples of cervical cancer tissues from 15 individual patients immediately after undergoing radical hysterectomy surgery. Among these cases, 11 were ADC types, with 5 being HPV-negative and 6 being HPV-positive. The remaining 4 cases were SCC types, with an even distribution of HPV-positive and HPV-negative status (**Supplementary Table 1**). Prior to surgery, all 15 patients were diagnosed as early FIGO stages (stage I ~IIA) based on evaluation of CT, MRI, and physical examination. However, after surgery, 5 cases turned out to be upstaged with pathological evidence of lymph node metastasis (FIGO stage IIICP), requiring theses patients to receive radiation therapy according to NCCN guidelines. Therefore, in addition to investigate the difference between histological types and HPV infection status, we also focused on the issue of post-surgical upstaging by comparing different FIGO stages.

In order to analyze the genomic profiling, we resolved these samples at the single-cell level using the 10X genomics chromium platform. The cell viability and sample quality were ensured beforehand, and a total of 102,012 qualified cells were utilized for further analysis (**Fig. 1A**). The technique of Uniform Manifold Approximation and Projection (UMAP) was utilized to reduce the dimension of gene

profiling data for visualization. The obtained cells were primarily categorized into 12 cell clusters, which were further re-clustered into 9 distinct cell types, based on specific gene markers (C. Li et al., 2022) (**Fig. 1B-C**). These cell types included T cells (38,627 cells in total, proportioning 37.87%, marked with PTPRC, CD3D, CD3E and CD3G), epithelial cells (32,199 cells in total, proportioning 31.56%, marked with EPCAM, SLP1 and CD24), neutrophils (12,586 cells in total, proportioning 12.34%, marked with CSF3R), macrophages (6,798 cells in total, proportioning 12.34%, marked with CD68 and CD163), fibroblasts (4,258 cells in total, proportioning 4.17%, marked with COL1A2 and DCN), plasma cells (4,044 cells in total, proportioning 3.96%, marked with JCHAIN), endothelial cells (1,389 cells in total, proportioning 1.36%, marked with ENG and VWF), B cells (1,326 cells in total, proportioning 1.30%, marked with CD79A and MS4A1) and mast cells (785 cells in total, proportioning 0.77%, marked with MS4A2) (**Fig. 1D-E** and **Supplementary Table 2**).

According to our scRNA-seq data, ADC exhibited a significant higher proportion of neutrophils than SCC (20.05% vs. 4.23%). The proportion of T cells was also higher in ADC (41.13%) compared to SCC (35.48%). Conversely, SCC showed a nearly threefold enrichment of epithelial cell (47.43%) compared to ADC (16.48%) (**Fig. 1F**). When considering the HPV infection status, HPV-negative patients demonstrated decreased proportions of epithelial cells (7.78% vs. 28.38%) and neutrophils (16.66% vs. 24.68%) compared to HPV-positive patients. The proportion of T cells enriched in HPV-negative cases (45.77%) was higher than that in HPV-positive cases (32.42%). HPV-negative patients exhibited prominently higher proportions of plasma cells (10.13% vs. 1.99%) and B cells (2.84% vs. 0.77%) compared to HPV-positive patients, even though their proportions were lower than T cells, epithelial cells and neutrophils (**Supplementary Fig. 1A**). Furthermore, we conducted a comparison between early-stage and late-stage cases, revealing that late-stage patients have a higher proportion of epithelial cells (35.50%) than

early-stage cases (28.82%) (**Supplementary Fig. 1B**). In summary, these data describes primarily a complex microenvironment in cervical cancers, especially in the ADC type, with varied composition of immune and tumor cells under different conditions.

The sub-clusters of epithelial cells exhibit elevated stem-like features to promote the aggressiveness of ADC

The aforehand data has shown that the majority of the CC tumor is composed of epithelial cells. In order to explore the characteristics of these epithelial cells within the TIME of ADC, we further classified them into 12 sub-clusters based on the subsets of differently expressed genes (DEGs) in each group (**Fig. 2A**). Each sub-cluster was named based on the most prominently up-regulated gene in each panel of signature genes (**Fig. 2B-C**). Several epithelial cell clusters were strongly enriched in ADC than SCC, such as Epi_04_TFF2, Epi_06_TMC5, Epi_07_CAPS and Epi_08_SCGB3A1. Notably, Epi_09_SST, Epi_10_CYSTM1, Epi_11_REG1A and Epi_12_RRAD were exclusively identified in ADC, not in SCC (**Fig. 2D**). The stratified enrichment of different cluster between ADC and SCC has captured our attention for further investigation. Additionally, Epi_09_SST, Epi_10_CYSTM1 and Epi_11_REG1A were solely enriched in HPV-positive cases, although no distinctive clusters had been found in HPV-negative patients (**Supplementary Fig. 2A**). When comparing samples from patients in the early stages with those who have lymph node metastasis, 3 clusters (Epi_02_IGLC2, Epi_05_CCL5 and Epi_12_RRAD) were slightly increased among the late-stage patients. Surprisingly, we found that the sub-cluster Epi_10_CYSTM1 was exclusively present in stage IIIC patients, making it a potential target for identification of the biomarkers for late stage patients (**Supplementary Fig. 2B**).

We further evaluated the features of each epithelial cluster, especially their roles in regulating tumorigenesis. To assess the differentiation potential of each cell cluster,

we employed the Cellular Trajectory Reconstruction Analysis using gene Counts and Expression (CytoTRACE) method (**Fig. 2E**). The results showed that clusters of Epi_07_CAPS, Epi_09_SST, Epi_10_CYSTM1 and Epi_12_RRAD ranked the top four in CytoTRACE score, indicating a significant potential for pluripotency and differentiation, also referred to stem-like features. Interestingly, Epi_09_SST, Epi_10_CYSTM1 and Epi_12_RRAD were exclusively enriched in ADC. The proportion of cluster Epi_07_CAPS, which acquired the highest level of stemness, was overwhelmingly higher in ADC, although Epi_07_CAPS was also identified in SCC (**Fig. 2D**). Subsequently, pseudotime analysis was conducted to elucidate the differentiation trajectories. The results showed that Epi_07_CAPS, Epi_09_SST and Epi_10_CYSTM1 were positioned towards the end of pseudotime developmental trajectory, which was in consistence with their high stem-like characteristics and indicated a higher degree of malignancy in ADC than SCC (**Supplementary Fig. 2C**). In addition, we performed the malignancy scoring analysis, which demonstrated that cluster Epi_10_CYSTM1 exhibited the highest degree of malignancy compared to other clusters (**Fig. 2F**). Interestingly, cluster Epi_10_CYSTM1 displayed a remarkably diverse developmental profile and was exclusively identified in ADC. Conversely, Epi_07_CAPS and Epi_12_RRAD, which exhibited high stem-like characteristics, were ranking lower in terms of malignancy scoring when compared to other clusters. This observation may partially indicate that high stemness cluster Epi_10_CYSTM1 is essential for ADC to present more aggressive features.

Next, we proceeded to further investigate cluster Epi_10_CYSTM1, particularly in the context of ADC. To this end, Gene Ontology Biological Process (GOBP) analysis on specific signaling pathways based on the gene expression pattern observed in each cell cluster was performed (**Fig. 2G** and **Supplementary Fig. 2D**). The results revealed that ADC-specific epithelial cell clusters, particularly the most malignant cluster Epi_10_CYSTM1, tended to be more active in regulating immunity-related pathways, which indicated epithelial sub-cluster might be associated with dysfunction

of immunity. Notably, Epi_10_CYSTM1 cluster also played a crucial role in regulating cell-to-cell interaction (**Fig. 2G**). This gives us a hint that ADC cells exert their tumor-promoting functions via interacting with other types of cells, such as neutrophils or immune cells. Therefore, further investigation is warranted to explore the intricate crosstalk networks between epithelial cells and other cell types.

ADC-specific epithelial cluster-derived gene SLC26A3 is a potential prognostic marker for lymph node metastasis

Given that Epi_10_CYTSM1 represents the most aggressive cell cluster in ADC, we further examined the relevance of this cluster and the clinical features of CC. As an alternative, we also examined Epi_12_RRAD (**Supplementary Fig. 3A**), which was another malignant cluster predominantly found in ADC. We firstly checked the DEGs of these two clusters. In Epi_12_RRAD cluster, we identified Insulin-like growth factor 2 (IGF2) and Alcohol dehydrogenase 1C (ADH1C), which were exclusively expressed in Epi_12_RRAD, as two most specific genes of this cluster (**Supplementary Fig. 3B**). However, the immunohistochemistry (IHC) staining showed that IGF2 was almost negative across cases with different clinical stages (**Supplementary Fig. 3C**). On the other hand, ADH1C was strongly expressed in both early-stage and late-stage cases (**Supplementary Fig. 3C**). Likewise, the survival analysis of Epi_12_RRAD-enriched gene signatures did not demonstrate a significant difference between the two groups (**Supplementary Fig. 3D**). These results suggest that the Epi_12_RRAD cluster may not play a significant role in the progression of ADC.

In contrast, the panel genes enriched in Epi_10_CYSTM1 might potentially predict poor prognosis of CC patients based on TCGA database (**Fig. 3C**). In the cluster of Epi_10_CYSTM1, the DEG with the highest expression is CYSTM1 (**Fig. 3A**). However, CYSTM1 was also expressed in other cell clusters and showed low specificity (**Fig. 3B**). On the other hand, SLC26A3, ORM1 and ORM2 were

specifically enriched in Epi_10_CYSTM1 and could be considered as potential candidate biomarkers for representation of this cluster. Nevertheless, ORM1/OMR2 were not satisfied to distinguish the severity of CC cases, due to an irrelevance between expression intensity and clinical stages (**Supplementary Fig. 3E**). Interestingly, the gene of SLC26A3 derived from Epi_10_CYSTM1 showed the most potential of prognostic value for CC patients (**Supplementary Fig. 3E**).

An important and unavoidable clinical issue in CC treatment is post-surgical upstaging, which affects the disease outcome and treatment approach. In order to examine the fact of post-surgical upstaging (or misdiagnose of early-stage cases), we merged data from two independent patient cohorts obtained from two clinical centers: Xiangya hospital (*Cohort 1*) and Hunan cancer hospital (*Cohort 2*). The criterion for objective selection was outlined below (**Supplementary Fig. 3F**). The rates of upstaging for each center are 10.85% (23 out of 212 in *Cohort 1*) and 15.31% (214 out of 1398 in *Cohort 2*), respectively. These rates fall within the range reported by previous studies (Dabi et al., 2018; Thelissen et al., 2022). Interestingly, both cohorts of data revealed that the misdiagnose rate was significantly higher in HPV-negative patients than HPV-positive patients, especially among ADC patients. From the data of *Cohort 2*, it was observed that ADC patients were more likely to stage up post-surgically. In *Cohort 1*, we can also observed the same tendency although without significant difference between different histological types, probably due to a smaller sample size (**Table. 1-2**).

The identification of Epi_10_CYSTM1 as the only cell cluster found in patients with stage IIICp raises the possibility that this cluster may be a potential marker to diagnose patients with lymph node metastasis. Therefore, we detected SLC26A3 expression on biopsy and post-surgical ADC samples to examine whether it was associated with lymph node metastasis. The results from IHC staining showed that ADC patients with stage IIIC had a higher expression of SLC26A3 (**Fig. 3D, E** and **Table 3, 4**). In summary, our results propose that the Epi_10_CYSTM1 cluster could

function as a diagnostic marker to predict both poor prognosis and lymph node metastasis in ADC patients. Moreover, SLC26A3 could be employed as a marker for the Epi_10_CYSTM1 cluster, aiding in the diagnosis of lymph node metastasis to prevent post-surgical upstaging in ADC patients in the future.

Enrichment of regulatory T cells indicates an immunosuppressive status of ADC

T cells play a crucial role as the primary effectors of tumor immunity. Our data reveals that T cells constitute the predominant cell population within the TIME of cervical cancer (**Fig. 1A**). A total of 52,297 T cells were categorized into 8 main clusters (**Fig. 4A**). The gene expression patterns of T cells in CC were in accord with those observed in other types of cancers (Sorin et al., 2023; Xue et al., 2022). Based on canonical genes (C. Li et al., 2022), these cells were re-clustered as the following 4 types of T cells: exhausted T cells (marked with CD8, TIGIT, PDCD1, LAG3, HAVCR2), cytotoxic T cells (marked with CD8 and CD3), regulatory T cells (Treg, marked with CD4, FOXP3 and IL2RA), activated T cells (marked with CD8, C69 and CD3G) (**Fig. 4A-C**). The gene subset of cytotoxic T cells exhibited a higher expression of KRT17, KRT19, while Tregs showed a higher expression of genes such as CCL4, GZMB and CCL3 (**Fig. 4D**). When comparing the checkpoint pathway states among different T cell clusters, we observed relatively higher levels of LAG3 and PDCD1 (PD1) in exhausted T cells, while CTLA4 and TIG1 were more highly expressed in Tregs. These genes were identified to present immunosuppressive functions (**Fig. 4E**). On the other hand, certain genes, such as NKG7, PRF1, INFG and TNFRSF, which indicate the activation of immune checkpoint pathways, exhibited low expression levels in cytotoxic T cells and activated T cells (**Fig. 4E)**. These findings lead us to hypothesize that the establishment of an immunosuppressive TIME in ADC may involve the recruitment of regulatory T cells (Tregs) to the tumor area and the subsequent inactivation of a substantial proportion of cytotoxic T cells.

We further compared different status of CC with different attribution of T cell

subtypes. It was demonstrated that ADC had a significantly higher proportion of Tregs compared to SCC (**Fig. 4F)**. Meanwhile, ADC patients who tested negative for HPV showed a higher enrichment of Tregs and a lower proportion of activated T cells compared to those with HPV-positive status (**Supplementary Fig. 4A**). These findings shed light on the underlying mechanism for immunotherapy insensitivity of ADC, especially in HPV-negative status. Furthermore, analyses of GOBP have shown that Tregs were more active in regulating immune activities in ADC than SCC, indicating a greater tendency for Tregs to be activated in the TIME of ADC (**Fig. 4G**). In ADC, the proportion of activated T cells was higher compared to SCC. However, the GOBP analysis suggested that their leading roles were to promote the apoptosis of immune cells than to exert cytotoxicity (**Supplementary Fig. 4D**). In addition, in HPV-negative cases, activated T cells demonstrated a stronger capacity to interact with other cell types, including neutrophils and epithelial cells (**Supplementary Fig. 4E**). Consequently, it is further proved that the enrichment of Tregs in ADC does execute immunosuppressive functions.

Tumor associated neutrophils (TANs) surrounding ADC tumor area contribute to the formation of a malignant microenvironment

The large-scale enrichment of specific gene subsets in neutrophils in CC prompted us to further examine their roles. A total of 12,586 neutrophils were detected and the composition proportion in ADC (20.05%) was almost five times higher than that in SCC (4.23%) (**Fig. 1F**). Based on this observation, we hypothesize that ADC-specific neutrophil clusters may be related to poor prognosis and increased malignancy. All the cells were initially grouped into 6 clusters based on the gene expression modules (**Fig. 5A**). In the context of cancer, tumor associated neutrophils (TANs) can exhibit dual functions, either promoting tumor (pro-tumor TANs) or inhibiting tumor progression (anti-tumor TANs). Based on the consensus markers identified by *Jaillon et al.* (Jaillon et al., 2020) and *Xue et al.*(Xue et al., 2022), we performed further clustering

of the neutrophils in our dataset, resulting in the identification of 3 sub-types of TANs: pro-tumor TANs (Neu_03, marked with CD66, CD11 and MT1X), anti-tumor TANs (Neu_02, marked with CD66, CD11, CCL5, KRT5 and ELF3), TANs with isg (interferon stimulated genes) and other undefined types (Neu_01, distinguished by CD66, CD11, IFITM2, S100A8 and LST1) (**Fig. 5B-C**). Generally, the Neu_01 sub-cluster, which consists of TANs with isg with the subset of specific genes, accounted for the largest proportion among all neutrophils. Notably, the presence of pro-tumor TANs was significantly higher in ADC compared to SCC (**Fig. 5D**), as well as in HPV-negative cases compared to HPV-positive cases (**Supplementary Fig. 5A**). On the other hand, the proportion of anti-tumor TANs in ADC was predominantly lower than that in SCC (**Fig. 5D**).

We further conducted the GOBP analysis on gene subsets derived from pro-tumor TANs to explore their potential functions. The findings revealed that pro-tumor TANs in ADC were more active in regulating cell-to-cell interactions and chemotaxis. Specifically, they were involved in pathways such as chemokine-mediated or cytokine-mediated signaling, neutrophil activation, and receptor internalization (**Fig. 5E**). These results suggest that pro-tumor TANs may engage in extensive communication with various cell types. Interestingly, pro-tumor TANs exhibited enhanced activation in mediating inhibitory pathways related to immunity (**Fig. 5E**). These pathways include the negative regulation of leukocyte proliferation and lymphocyte activation, as well as the suppression of IL-10 production, which is known to promote immune responses (Saraiva, Vieira, & O'Garra, 2020; Sarvaria, Madrigal, & Saudemont, 2017).

The role of pro-tumor TANs in association with disease prognosis was further verified using TCGA database. The patients with higher expression of gene panels specific to pro-tumor TANs exhibited a poorer prognosis compared to those with lower expression (**Fig. 5F**). These findings suggest that the increased malignancy observed in ADC, particularly in HPV-negative cases, may also be attributed to the

enrichment of pro-tumor TANs and evasion of anti-tumor TANs.

Cellular heterogeneity of plasma/B cells in ADC

In our study, we identified 6 distinctive clusters of plasma/B cells based on the set of gene enrichment: Plasma/B_01(marked with IGHA2, IGHG2 and IGLC2), Plasma/B_02 (marked with HLA-DRA, HLA-DPB and CD37), Plasma/B_03 (marked with KRT17 and S100A2), Plasma/B_04 (marked with CCL5, CXCL13, IL-32 and CCL4), Plasma/B_05 (marked with CXCL8), Plasma/B_06 (marked with HMGB2) (**Fig. 6A-C**). Among these clusters, the most abundant one was Plasma/B_01_IGHA2 (**Fig. 6D** and **Supplementary Fig. 6A-B**). Interestingly, the proportion of Plasma/B_01_IGHA2 was found to be significantly higher in ADC compared to SCC, and it was also slightly higher in HPV-negative cases than in HPV-positive cases (**Fig. 6D** and **Supplementary Fig. 6A**). Generally, B-lymphocytes are known to have tumor-inhibitory properties. However, the ectopic gene module of plasma/B cells in ADC suggested that some sub-clusters might present a tumor-promoting role. This hypothesis was further supported by the results of GOBP analysis, which indicated that Plasma/B_01_IGHA2 gene signatures were more active in negatively regulating B cell activation, complement activation and receptor signaling pathway (**Fig. 6E**). When we combined the top 50 signature genes in Plasma/B_01_IGHA2-enriched subset and performed the survival analysis using TCGA database, we observed that higher expression of the signature genes predicted a poorer prognosis of CC patients (**Fig. 6F**). Taken together, the cellular heterogeneity of plasma/B cells in the TIME of ADC is well identified at the single-cell level.

Crosstalk among tumor cells, Tregs and neutrophils establishes the immunosuppressive TIME in ADC

In the above description, we have outlined that certain ADC-enriched cell sub-clusters, such as Epi_10_CYSTM1, Tregs, and pro-tumor TANs, played

oncogenic roles in regulating various cellular activities, including maintenance of stemness and evasion of immune surveillance. To gain deeper insights into the interplay among these clusters and their influence on ADC progression, we harnessed the Cellchat tool (Jin et al., 2021). Our primary focus revolved around unraveling the mechanisms governing Treg recruitment to the tumor microenvironment and the maintenance of stemness within ADC-enriched cell sub-clusters.

Given that the 3 ADC-specific sub-clusters (Epi_07_CAPS, Epi_10_CYSTM1 and Epi_12_RRAD) of epithelial cells exhibited quite high levels of stem-like properties, and particularly that Epi_10_CYSTM1 presented the highest degree of malignancy among them, we further analyzed their interactions with other types of cells. Firstly, in comparison to SCC, ADC-enriched epithelial sub-clusters exhibited a higher propensity for interaction with Tregs through ligand-receptor signaling pathways, including ALCAM (ALCAM>>CD6) and MHC-II (HLA-DR>>CD4) (**Fig. 7A-E**), which have been reported to be essential for Treg recruitment, expansion and stabilization to establish the immunosuppressive microenvironment (Chalmers et al., 2022; Ferragut, Vachetta, Troncoso, Rabinovich, & Elola, 2021; Freitas et al., 2019). To further uncover the underlying reason for the enhanced stemness observed in ADC epithelial cells, we focused on the signaling received by Epi_10_CYSTM1 cell cluster. Interestingly, the Cellchat analysis revealed that, compared to other pathways, such as CD46>>JAG1 and GZMA>>PARD3, the interaction of TGFβ>>TGFBR between Tregs and epithelial cells (particularly in cluster Epi_10_CYSTM1) was remarkedly activated in ADC but not in SCC (**Fig. 7F-G**). TGFβ is a canonical secreted protein that induces carcinogenesis, such as cancer cell proliferation, invasion and self-renewal (Derynck, Turley, & Akhurst, 2021; Massagué, 2008; Tauriello, Sancho, & Batlle, 2022). Thus, we speculate that the recruited Tregs might secrete TGFβ to stimulate the tumor epithelial cells of ADC, leading to increased stemness. Additionally, pro-tumor TANs were also recruited to the tumor area and interacted with Epi_10_CYSTM1, as well as Epi_07_CAPS and Epi_12_RRAD cells, via the

ANNEXIN-to-FPR1/FPR2 signaling pathway (**Supplementary Fig. 7A-B**). Previous studies have reported that the ANNEXIN pathway can promote the chemotaxis of neutrophils (Araújo et al., 2021). Likewise, TANs expressing isg, which have been shown to promote tumorigenesis as mentioned earlier, were also recruited to the tumor area through the ANNEXIN pathway. These findings suggest that the aggressive clusters of TANs may contribute to the formation of an ADC-specific TIME.

To approve these hypotheses, we conducted immunofluorescence (IF) analysis and observed a greater recruitment of $FOXP3^{+}$ cells in close proximity to regions exhibiting high SLC26A3 expression (Epi_10_CYSTM1 cell cluster) (**Fig. 7H**). Furthermore, when compared to regions with low SLC26A3 expression, tumors displaying high SLC26A3 levels exhibited significantly increased expression of Aldehyde Dehydrogenase 1 Family Member A1 (ALDH1A1), a known marker for cancer stem cells in CC (Douville, Beaulieu, & Balicki, 2009) (**Supplementary Fig. 7C**). Notably, we identified $SLC26A3^{high}$ tumor cells expressing ALCAM in close proximity to CD6+ Tregs, suggesting potential involvement of ALCAM>>CD6 signaling in Treg recruitment (**Fig. 7I**). Additionally, we observed reduced E-cadherin expression in tumor cells within SLC26A3high regions, possibly induced by TGFβ secreted by adjacent Tregs (**Fig. 7J** and **Supplementary Fig. 7D**). Altogether, these findings confirm the intricate crosstalk between the Epi_10_CYSTM1 cell cluster and Tregs, which plays a pivotal role in establishing an immunosuppressive TIME and sustaining heightened stemness in tumor cells.

Discussion

Cervical cancer is often regarded as less aggressive compared to ovarian cancer and endometrial cancer, primarily due to the effectiveness of HPV vaccines in prevention. When diagnosed at early stages, the 5-year survival rate for cervical cancer patients exceeds 90%, surpassing that of other gynecologic malignancies (Gennigens et al.,

2022; Schiffman, Castle, Jeronimo, Rodriguez, & Wacholder, 2007). However, if cervical cancer metastasizes to the intraperitoneal or retroperitoneal lymph nodes, the survival rate will decrease to 30%~60% (Cohen et al., 2019). Worse still, the 5-year survival rate for recurrent CC patients is less than 20% (H. Li, Wu, & Cheng, 2016). Specifically, when considering the ADC type alone, the prognosis is even worse. Unfortunately, our understanding for ADC is limited. Most previous studies have concentrated on SCC type of CC, and obtained heterogenetic information derived from bulk RNA-seq method. Therefore, it is worthwhile to shift our attention towards an in-depth investigation on the disparities between ADC and SCC at the single-cell resolution.

More recently, researchers have started to utilize scRNA-seq approach to investigate the tumor microenvironment of CC. For instance, Cao *et al* compared 5 cases of SCC tumor tissues with paired adjacent normal tissues and described the immune landscape in which specific clusters of T and B cells exhibited immune-exhausting or activating processes (Cao et al., 2023). Another study conducted by *Qiu et al* aimed to elucidate the distinct molecular patterns of immune reactions between ADC and SCC in the context of different HPV infection status at the single-cell level (Qiu et al., 2023). However, due to limited samples tested in these studies, our knowledge on the TIME in CC is yet inadequate. In the current study, we have generated a genomic atlas of ADC, which may depict the landscape of TIME built by both ADC tumor cells and neighboring cells. Apart from the predominant presence of epithelial cells, the cell clusters in ADC are majorly composed of T cells, tumor-associated neutrophils (TANs), and plasma/B cells. The gene subsets identified within ADC-abundant cell sub-clusters, including Epi_10_CYSTM1, Tregs, pro-tumor TANs and P/B_01_IGHA2, exert potential roles in promoting both the carcinogenesis and immunosuppression of ADC. In the TIME of ADC, the unique module of cellular interaction has been decoded and validated that the immunosuppressive Tregs and the tumor-promoting TANs are recruited to tumor cells

via chemo-attraction. Finally, our hypothesis from scRNA-seq data is further confirmed using clinical samples, providing evidence that SLC26A3 is a reliable biomarker for ADC (**Supplementary Fig. 8**).

It has been reported that immunotherapies are less effective on ADC patients, especially those who are not infected with HPV (Attademo et al., 2020; Ferrall, Lin, Roden, Hung, & Wu, 2021). As the two major components of ADC cell types, T cells and epithelial cells have been shown to be the dominant regulators in the TIME due to their reciprocal interaction dynamics. We identified several ADC-specific epithelial cell clusters that exhibit strong stemness and aggressiveness. Among these clusters, Epi_10_CYSTM1 demonstrated the highest level of malignancy, but the underlying mechanism behind this behavior remains unknown. The Cellchat analysis revealed that Tregs might quite actively crosstalk to Epi_10_CYSTM1. To confirm this, immunostaining for co-localization demonstrated an increased aggregation of Tregs around tumor cells exhibiting overexpression of SLC26A3. It has also been widely reported that tumor cells acquire higher stemness present more aggressive features of resistance to immunotherapy (Dianat-Moghadam et al., 2022). This study confirmed that TGFβ produced by Tregs induce the stemness of Epi_10_CYSTM1 cells by activating downstream oncogenic pathways, inducing EMT on tumor epithelial cells (Nixon, Gao, Wang, & Li, 2023). Interestingly, Epi_10_CYSTM1 cells express ALCAM, which is a soluble ligand, and bind to its receptor CD6 on Tregs, activating chemotaxis and facilitating Treg recruitment. The infiltration of a large number of Tregs in ADC significantly accelerates immune evasion (**Supplementary Fig. 8**). Therefore, the presence of a higher number of Tregs infiltrating the tumor area of ADC may explain the increased resistance to immunotherapy. It is worth noting that, in comparison to the proportions of Tregs, the majority of T cell fractions in the CC tumor area are comprised of cytotoxic T cells and exhausted T cells. However, their distribution is relatively equal, indicating the dysfunctional status of the majority of infiltrated T cells in the CC tumor area.

Another interesting phenomenon observed in our sing-cell sequencing data is the involvement of TANs in the regulatory interactions within the TIME of ADC. It has been clearly investigated that pro-tumor TANs, characterized by CD66, CD11, CD170 and PD-L1, exert the oncogenic roles by promoting tumor cell proliferation, angiogenesis, inducing genetic instability, and most importantly causing immunosuppression (Jaillon et al., 2020). In this study, pro-tumor TANs are predominantly enriched in ADC tissues compared to SCC, especially in HPV-negative ADC cases. This suggests that ADC-specific epithelial cell sub-clusters actively engage in the recruitment of pro-tumor TANs through the ANXA1-FPR1/FPR2 ligand-receptor interaction.

The anti-tumor function of B cells has been identified previously (Bod et al., 2023; Helmink et al., 2020). However, our study has presented a specific cluster of plasma/B cells with tumor-promoting functions. The overexpression of gene signatures from Plasma/B_01_IGH2 cells is associated with poor regression in CC patients. Interestingly, Plasma/B_01-IGHA2 was found to be closely related to the PC Cluster (Plasma cell Cluster) in Cao's study due to the shared gene set (Cao et al., 2023), such as IGHA1, IGHA2, IGHG2, IGHG4, *etc.* However, their roles were contradictory. According to that study, PC cluster was derived from the local expansion of TIME and showed potential effectiveness in anti-tumor immunity. In our case, Plasma/B_01-IGHA2 had a reverse effect and played a tumor-promoting role in ADC. This difference in function is likely attributed to the distinct cell types and their interactions in ADC, instead of SCC. Although the cell-to-cell interaction did not yield positive results, probably owing to the small cell proportion, the underneath dynamics of B cells still need further investigation.

Most importantly, in this study SLC26A3 is identified as a promising diagnostic biomarker to predict lymph node metastasis in ADC patients at stage IIIC. In 2018, the International Federation of Gynecology and Obstetrics (FIGO) updated a new criterion of stage IIIC by including lymph node status, which indicates that the

therapeutic strategy is completely different from early stages. There are two stratification of stage IIIC: IIICp (p stands for pathological findings of LN, which means misdiagnosis) and IIICr (r stands for radiological findings of LN, which means pre-surgical evidence) (Bhatla, Aoki, Sharma, & Sankaranarayanan, 2018). Unfortunately, radiological imaging tools do have some limitations, as CT or MRI can only detect suspiciously metastatic LN when the minimum diameter is ≥ 10mm (Saleh et al., 2020). However, over 10% of CC patients who are initially diagnosed with early-stage and deemed suitable for radical surgery, end up being upstaged due to lymph node metastasis discovered after the surgery (Dabi et al., 2018; Thelissen et al., 2022). For these patients, they require additional radiotherapy such as external beam irradiation besides surgery (Abu-Rustum et al., 2020). However, if the presence of lymph node metastasis could have been accurately diagnosed in biopsy sample, the optimal therapeutic approach for these patients would be radiotherapy alone. Moreover, combination of both surgery and radiotherapy may lead to more complications for patients than radiotherapy alone, without offering additional benefits (Cushman et al., 2018; Kashima et al., 2023; J. Yang et al., 2015). To solve this problem, a reliable biomarker is required to diagnose LN metastasis in conjunction with radiographic tool. Combining two large cohorts of clinical data, we identified that CC patients with ADC types were more vulnerable to be misdiagnosed for clinical staging. Derived from scRNA-seq data, SLC26A3 could be employed as a marker for the Epi_10_CYSTM1 cluster, which was found to be exclusively enriched in stage IIIC cases of ADC. The IHC staining further confirmed that ADC patients at stage IIIC exhibited higher expression of SLC26A3 compared to early stages (FIGO stage I~ II). Furthermore, we tested on biopsy samples and it implied that SLC26A3 could be a significant predictor of LN metastasis. Our study for the first time provides evidence that ADC patients are at a higher risk of developing lymph node metastasis, which can be challenging to detect solely through radiological imaging techniques. However, by incorporating lymph node imaging with biomarkers such as SLC26A3, it

may significantly reduce the misdiagnosis rate among FIGO IIICp patients.

In summary, we characterized the genomic landscape of the TIME in ADC at a single-cell resolution. Our study revealed the presence of specific epithelial cell clusters in ADC that exhibited high aggressiveness. The enriched gene signatures within these clusters may serve as potential therapeutic targets to improve the efficacy of immunotherapy. The interactions between tumor epithelial cells and other types of cells, such as T cells and neutrophils, comprehensively depict a highly immunosuppressive microenvironment of ADC. Moreover, our investigation extended to the issue of upstaging at the single-cell level, with the identification of potential biomarkers from specific tumor cell clusters showing promise as diagnostic indicators for the precise diagnosis of cervical cancer patients.

References

Abu-Rustum, N. R., Yashar, C. M., Bean, S., Bradley, K., Campos, S. M., Chon, H. S., . . . Motter, A. D. (2020). NCCN Guidelines Insights: Cervical Cancer, Version 1.2020. *J Natl Compr Canc Netw, 18*(6), 660-666. doi:10.6004/jnccn.2020.0027

Araújo, T. G., Mota, S. T. S., Ferreira, H. S. V., Ribeiro, M. A., Goulart, L. R., & Vecchi, L. (2021). Annexin A1 as a Regulator of Immune Response in Cancer. *Cells, 10*(9). doi:10.3390/cells10092245

Attademo, L., Tuninetti, V., Pisano, C., Cecere, S. C., Di Napoli, M., Tambaro, R., . . . Pignata, S. (2020). Immunotherapy in cervix cancer. *Cancer Treat Rev, 90*, 102088. doi:10.1016/j.ctrv.2020.102088

Bhatla, N., Aoki, D., Sharma, D. N., & Sankaranarayanan, R. (2018). Cancer of the cervix uteri. *Int J Gynaecol Obstet, 143 Suppl 2*, 22-36. doi:10.1002/ijgo.12611

Bod, L., Kye, Y. C., Shi, J., Torlai Triglia, E., Schnell, A., Fessler, J., . . . Kuchroo, V. K. (2023). B-cell-specific checkpoint molecules that regulate anti-tumour immunity. *Nature, 619*(7969), 348-356. doi:10.1038/s41586-023-06231-0

Cao, G., Yue, J., Ruan, Y., Han, Y., Zhi, Y., Lu, J., . . . Li, F. (2023). Single-cell dissection of cervical cancer reveals key subsets of the tumor immune microenvironment. *Embo j, 42*(16), e110757. doi:10.15252/embj.2022110757

Chalmers, S. A., Ayilam Ramachandran, R., Garcia, S. J., Der, E., Herlitz, L., Ampudia, J., . . . Putterman, C. (2022). The CD6/ALCAM pathway promotes lupus nephritis via T cell-mediated responses. *J Clin Invest, 132*(1). doi:10.1172/jci147334

Cohen, P. A., Jhingran, A., Oaknin, A., & Denny, L. (2019). Cervical cancer. *Lancet, 393*(10167), 169-182. doi:10.1016/s0140-6736(18)32470-x

Colombo, N., Dubot, C., Lorusso, D., Caceres, M. V., Hasegawa, K., Shapira-Frommer, R., . . . Monk, B. J. (2021). Pembrolizumab for Persistent, Recurrent, or Metastatic Cervical Cancer. *N Engl J Med, 385*(20), 1856-1867. doi:10.1056/NEJMoa2112435

Cushman, T. R., Haque, W., Menon, H., Rusthoven, C. G., Butler, E. B., Teh, B. S., & Verma, V. (2018). Postoperative chemoradiotherapy versus radiotherapy alone for elderly cervical cancer patients with positive margins, lymph nodes, or parametrial invasion. *J Gynecol Oncol, 29*(6), e97. doi:10.3802/jgo.2018.29.e97

Dabi, Y., Simon, V., Carcopino, X., Bendifallah, S., Ouldamer, L., Lavoue, V., . . . Touboul, C. (2018). Therapeutic value of surgical paraaortic staging in locally advanced cervical cancer: a multicenter cohort analysis from the FRANCOGYN study group. *J Transl Med, 16*(1), 326. doi:10.1186/s12967-018-1703-4

Derynck, R., Turley, S. J., & Akhurst, R. J. (2021). TGFβ biology in cancer progression and immunotherapy. *Nat Rev Clin Oncol, 18*(1), 9-34. doi:10.1038/s41571-020-0403-1

Dianat-Moghadam, H., Mahari, A., Salahlou, R., Khalili, M., Azizi, M., & Sadeghzadeh, H. (2022). Immune evader cancer stem cells direct the perspective approaches to cancer immunotherapy. *Stem Cell Res Ther, 13*(1), 150. doi:10.1186/s13287-022-02829-9

Douville, J., Beaulieu, R., & Balicki, D. (2009). ALDH1 as a functional marker of cancer stem and progenitor cells. *Stem Cells Dev, 18*(1), 17-25. doi:10.1089/scd.2008.0055

Fernandes, A., Viveros-Carreño, D., Hoegl, J., Ávila, M., & Pareja, R. (2022). Human papillomavirus-independent cervical cancer. *Int J Gynecol Cancer, 32*(1), 1-7. doi:10.1136/ijgc-2021-003014

Ferragut, F., Vachetta, V. S., Troncoso, M. F., Rabinovich, G. A., & Elola, M. T. (2021). ALCAM/CD166: A pleiotropic mediator of cell adhesion, stemness and cancer progression. *Cytokine Growth Factor Rev, 61*, 27-37. doi:10.1016/j.cytogfr.2021.07.001

Ferrall, L., Lin, K. Y., Roden, R. B. S., Hung, C. F., & Wu, T. C. (2021). Cervical Cancer Immunotherapy: Facts and Hopes. *Clin Cancer Res, 27*(18), 4953-4973. doi:10.1158/1078-0432.ccr-20-2833

Freitas, R. F., Basto, A., Almeida, S. C. P., Santos, R. F., Gonçalves, C. M., Corria-Osorio, J., . . . Graca, L. (2019). Modulation of CD4 T cell function via CD6-targeting. *EBioMedicine, 47*, 427-435. doi:10.1016/j.ebiom.2019.08.008

Gennigens, C., Jerusalem, G., Lapaille, L., De Cuypere, M., Streel, S., Kridelka, F., & Ray-Coquard, I. (2022). Recurrent or primary metastatic cervical cancer: current and future treatments. *ESMO Open, 7*(5), 100579.

doi:10.1016/j.esmoop.2022.100579

Guo, W., Wang, D., Wang, S., Shan, Y., Liu, C., & Gu, J. (2021). scCancer: a package for automated processing of single-cell RNA-seq data in cancer. *Brief Bioinform, 22*(3). doi:10.1093/bib/bbaa127

Helmink, B. A., Reddy, S. M., Gao, J., Zhang, S., Basar, R., Thakur, R., . . . Wargo, J. A. (2020). B cells and tertiary lymphoid structures promote immunotherapy response. *Nature, 577*(7791), 549-555. doi:10.1038/s41586-019-1922-8

Jaillon, S., Ponzetta, A., Di Mitri, D., Santoni, A., Bonecchi, R., & Mantovani, A. (2020). Neutrophil diversity and plasticity in tumour progression and therapy. *Nat Rev Cancer, 20*(9), 485-503. doi:10.1038/s41568-020-0281-y

Jin, S., Guerrero-Juarez, C. F., Zhang, L., Chang, I., Ramos, R., Kuan, C. H., . . . Nie, Q. (2021). Inference and analysis of cell-cell communication using CellChat. *Nat Commun, 12*(1), 1088. doi:10.1038/s41467-021-21246-9

Kashima, Y., Murakami, K., Miyagawa, C., Takaya, H., Kotani, Y., Nakai, H., & Matsumura, N. (2023). Treatment for Locally Resectable Stage IIIC1 Cervical Cancer: A Retrospective, Single-Institution Study. *Healthcare (Basel), 11*(5). doi:10.3390/healthcare11050632

Li, C., Wu, H., Guo, L., Liu, D., Yang, S., Li, S., & Hua, K. (2022). Single-cell transcriptomics reveals cellular heterogeneity and molecular stratification of cervical cancer. *Commun Biol, 5*(1), 1208. doi:10.1038/s42003-022-04142-w

Li, H., Wu, X., & Cheng, X. (2016). Advances in diagnosis and treatment of metastatic cervical cancer. *J Gynecol Oncol, 27*(4), e43. doi:10.3802/jgo.2016.27.e43

Lv, B., Wang, Y., Ma, D., Cheng, W., Liu, J., Yong, T., . . . Wang, C. (2022). Immunotherapy: Reshape the Tumor Immune Microenvironment. *Front Immunol, 13*, 844142. doi:10.3389/fimmu.2022.844142

Mann, M., Singh, V. P., & Kumar, L. (2023). Cervical cancer: a tale from HPV infection to PARP inhibitors. *Genes Dis, 10*(4), 1445-1456. doi:10.1016/j.gendis.2022.09.014

Massagué, J. (2008). TGFbeta in Cancer. *Cell, 134*(2), 215-230. doi:10.1016/j.cell.2008.07.001

Nixon, B. G., Gao, S., Wang, X., & Li, M. O. (2023). TGFβ control of immune responses in cancer: a holistic immuno-oncology perspective. *Nat Rev Immunol, 23*(6), 346-362. doi:10.1038/s41577-022-00796-z

Omenai, S. A., Ajani, M. A., & Okolo, C. A. (2022). Programme death ligand 1 expressions as a surrogate for determining immunotherapy in cervical carcinoma patients. *PLoS One, 17*(2), e0263615. doi:10.1371/journal.pone.0263615

Peng, Y., Kajiyama, H., Yuan, H., Nakamura, K., Yoshihara, M., Yokoi, A., . . . Kikkawa, F. (2019). PAI-1 secreted from metastatic ovarian cancer cells triggers the tumor-promoting role of the mesothelium in a feedback loop to accelerate peritoneal dissemination. *Cancer Lett, 442*, 181-192.

doi:10.1016/j.canlet.2018.10.027

Qiu, J., Qu, X., Wang, Y., Guo, C., Lv, B., Jiang, Q., . . . Hua, K. (2023). Single-Cell Landscape Highlights Heterogenous Microenvironment, Novel Immune Reaction Patterns, Potential Biomarkers and Unique Therapeutic Strategies of Cervical Squamous Carcinoma, Human Papillomavirus-Associated (HPVA) and Non-HPVA Adenocarcinoma. *Adv Sci (Weinh), 10*(10), e2204951. doi:10.1002/advs.202204951

Saleh, M., Virarkar, M., Javadi, S., Elsherif, S. B., de Castro Faria, S., & Bhosale, P. (2020). Cervical Cancer: 2018 Revised International Federation of Gynecology and Obstetrics Staging System and the Role of Imaging. *AJR Am J Roentgenol, 214*(5), 1182-1195. doi:10.2214/ajr.19.21819

Saraiva, M., Vieira, P., & O'Garra, A. (2020). Biology and therapeutic potential of interleukin-10. *J Exp Med, 217*(1). doi:10.1084/jem.20190418

Sarvaria, A., Madrigal, J. A., & Saudemont, A. (2017). B cell regulation in cancer and anti-tumor immunity. *Cell Mol Immunol, 14*(8), 662-674. doi:10.1038/cmi.2017.35

Sasieni, P., Castanon, A., & Cuzick, J. (2009). Screening and adenocarcinoma of the cervix. *Int J Cancer, 125*(3), 525-529. doi:10.1002/ijc.24410

Schiffman, M., Castle, P. E., Jeronimo, J., Rodriguez, A. C., & Wacholder, S. (2007). Human papillomavirus and cervical cancer. *Lancet, 370*(9590), 890-907. doi:10.1016/s0140-6736(07)61416-0

Sorin, M., Rezanejad, M., Karimi, E., Fiset, B., Desharnais, L., Perus, L. J. M., . . . Walsh, L. A. (2023). Single-cell spatial landscapes of the lung tumour immune microenvironment. *Nature, 614*(7948), 548-554. doi:10.1038/s41586-022-05672-3

Sun, J. Y., Zhang, D., Wu, S., Xu, M., Zhou, X., Lu, X. J., & Ji, J. (2020). Resistance to PD-1/PD-L1 blockade cancer immunotherapy: mechanisms, predictive factors, and future perspectives. *Biomark Res, 8*, 35. doi:10.1186/s40364-020-00212-5

Sung, H., Ferlay, J., Siegel, R. L., Laversanne, M., Soerjomataram, I., Jemal, A., & Bray, F. (2021). Global Cancer Statistics 2020: GLOBOCAN Estimates of Incidence and Mortality Worldwide for 36 Cancers in 185 Countries. *CA Cancer J Clin, 71*(3), 209-249. doi:10.3322/caac.21660

Tauriello, D. V. F., Sancho, E., & Batlle, E. (2022). Overcoming TGFβ-mediated immune evasion in cancer. *Nat Rev Cancer, 22*(1), 25-44. doi:10.1038/s41568-021-00413-6

Thelissen, A. A. B., Jürgenliemk-Schulz, I. M., van der Leij, F., Peters, M., Gerestein, C. G., Zweemer, R. P., & van Rossum, P. S. N. (2022). Upstaging by para-aortic lymph node dissection in patients with locally advanced cervical cancer: A systematic review and meta-analysis. *Gynecol Oncol, 164*(3), 667-674. doi:10.1016/j.ygyno.2021.12.026

Vinay, D. S., Ryan, E. P., Pawelec, G., Talib, W. H., Stagg, J., Elkord, E., . . . Kwon, B.

S. (2015). Immune evasion in cancer: Mechanistic basis and therapeutic strategies. *Semin Cancer Biol, 35 Suppl*, S185-s198. doi:10.1016/j.semcancer.2015.03.004

Xue, R., Zhang, Q., Cao, Q., Kong, R., Xiang, X., Liu, H., . . . Zhang, N. (2022). Liver tumour immune microenvironment subtypes and neutrophil heterogeneity. *Nature, 612*(7938), 141-147. doi:10.1038/s41586-022-05400-x

Yang, J., Ding, C., Zhang, T., Zhang, L., Lv, T., Ge, X., . . . Li, J. (2015). Clinical features, outcome and risk factors in cervical cancer patients after surgery for chronic radiation enteropathy. *Radiat Oncol, 10*, 128. doi:10.1186/s13014-015-0433-5

Yang, X., Li, Y., Tang, Y., Li, Z., Wang, S., Luo, X., . . . Luo, M. (2023). Cervical HPV infection in Guangzhou, China: an epidemiological study of 198,111 women from 2015 to 2021. *Emerg Microbes Infect, 12*(1), e2176009. doi:10.1080/22221751.2023.2176009

Additional information

Funding

Funder	Grant reference number	Author
National Natural Science Foundation of China	82002753	Yang Peng
Natural Science Foundation of Hunan Province	2021JJ40324	Yang Peng
National Natural Science Foundation of China	82072882	Congrong Liu

Author contributions

Yang Peng, Conceptualization, Methodology, Formal analysis, Investigation, Data curation, Visualization, Writing – original draft preparation, Project administration, Funding acquisition; Yilin Li, Methodology, Validation, Investigation, Resources, Data curation, Visualization; Jixing Ao, Methodology, Validation, Software, Resources, Investigation, Data curation; Jia Shen, Software, Validation, Investigation, Data curation, Visualization; Xiang He, Software, Investigation, Data curation, Visualization; Dihong Tang, Methodology, Formal analysis, Writing – review & editing; Chaonan Chu, Formal analysis, Writing – review & editing; Congrong Liu,

Conceptualization, Methodology, Formal analysis, Writing – review & editing, Supervision, Project administration, Funding acquisition; Liang Weng, Conceptualization, Methodology, Software, Validation, Formal analysis, Investigation, Writing – original draft preparation, Writing – review & editing, Supervision, Project administration.

Ethics approval and consent to participate

Specimen collection and pathological data used in this study were approved by the Ethics Committee of Hunan Cancer Hospital (No. KYJJ-2020-036). Written informed consent was obtained from patients for use of samples. This study was also in accordance with the Declaration of Helsinki and none of any procedures conducted interfered with the treatment plan of patients.

Data availability

In this study, the single-cell RNA sequencing data generated is available in the Genome Sequence Archive for Human (GSA-Human, from China National Center for Bioinformation) by accession number: PRJCA023028 (https://ngdc.cncb.ac.cn/gsa-human/). These original sequencing data can be obtained only for non-profitable use, under request from the corresponding authors.

Competing interests

All authors declare no competing interests of publication.

Figure legends

Figure 1. The single-cell genomic atlas of cervical cancer. A. The schematic design of sample collection, single-cell RNA sequencing, data processing and clinical validating through 10X genomics platform. The sketch of scRNA-sq machine, as well as the plot of dimension-reduction visualization, was originally cited from the official website of 10X genonics: https://www.10xgenomics.com. **B.** UMAP plots of all single cells by original clustering and cell type re-clustering, according to the published lineage-specific marker genes, respectively. **C.** Violin plots demonstrating the expression of marker genes that correspond to each of the major cell types. **D.** UMAP plots demonstrating the most typical marker gene specific to each type of cell cluster. **E.** UMAP plot and histogram plot showing the occupation ratios of the major cell types in each individual sample, with HPV status and histological type summarized. **F.** UMAP (up) and histogram (down) plots to show the differences of distribution and proportion of each cell type between different histological types (ADC vs. SCC).

Figure 2. The scRNA-seq data reveals the malignant features of tumor epithelial cells. A. UMAP plots showing the distribution of epithelial cells in 15 samples and the sub-clustering into 12 clusters according to ectopic gene expressions. Each cluster of epithelial cells was named using the most highly enriched gene. **B.** Heatmap plot showing the annotation of each epithelial sub-cluster with top 5 DEGs. **C.** UMAP plots demonstrating the most specific gene as the marker for each sub-cluster. **D.** UMAP (left) and histogram (right) plots to compare the differences of distribution and proportion of each epithelial cell sub-cluster between different histological types (ADC vs. SCC). **E.** UMAP plot of CytoTRACE showing the thermal imaging projection of predicted developmental order (left) and histogram plot showing the ranking of CytoTRACE scores (right). **F.** UMAP plot of malignancy analysis demonstrating the cell malignancy features (up) and ranking of scores (down). **G.** GOBP analyses showing the top 15 enriched signaling pathways of Epi_10_CYSTM1

that are more active in ADC than SCC (up), particularly pathways related to cell-to-cell interactions (down). The histogram data are transformed from -Log_{10}(*P*-value) for visualization. ***Abbreviations:*** Ig: immunoglubolin; MHC: major histocompatibility complex.

Figure 3. SLC26A3 is identified as a potential prognostic and diagnostic indicator for lymph node metastasis of CC patients. A. Heatmap showing the top 50 DEGs of Epi_10_CYSTM1 cluster in comparison to all the other sub-clusters (Red: Epi_10_CYSTM1 cluster; Green: other epithelial cell sub-clusters). **B.** Violin plots showing the expression difference between two groups (top), with UMAP plots (bottom) demonstrating the specificity of each candidate gene, filtering SLC26A3 as the most identical marker for this sub-cluster. **C.** Kaplan-Meier curve showing the overall survival rates of CC patients stratified by the top 50 genes-scaled signature of Epi_CYSTM1. **D.** IHC staining showing the protein expression of SLC26A3 in surgically-resected ADC samples which are classified as early stages (FIGO stage I-IIA) and late stages (FIGO stage IIIC1~2p). Images from 6 individual cases were shown as representatives for each group. **E.** IHC staining showing the protein expression of SLC26A3 in biopsy ADC samples which are classified as early stages (FIGO stage I-IIA) and late stages (FIGO stage IIIC1~2p). Images from 4 individual cases were shown as representatives for each group. The method of *H*-score is used and the scoring system is as follows: negative (0), weak (1), intermediate (2), and strong (3). Expression is quantified by the H-score method.

Figure 4. Cellular and molecular heterogeneity of T cells in ADC. A. UMAP plots showing the sample distribution (left), original cell clustering of T cells (middle, 8 clusters in total) and re-clustering of T cell subtypes (right, 4 major sub-clusters: exhausted T cell, cytotoxic T cell, regulatory T cell and activated T cell) according to acknowledged marker genes. **B.** Violin plot showing the expression of specific marker

genes that annotate each sub-type of T cells. **C.** UMAP plots showing the widely recognized classification markers that denote each type of T cell sub-cluster. **D.** Dot heatmap plot of row-scaled expression of overexpressed genes for each sub-cluster of T cells. **E.** Dot heatmap plots that demonstrate the level of marker genes representing the signaling pathways of immune checkpoint activation and inhibition for grouped sub-clusters. **F.** Differences of distribution and proportion of each T cell sub-cluster between different histological types (ADC vs. SCC). **G.** GOBP analysis of Treg-enriched immunity-related pathways that are more active in ADC than SCC. The histogram data are transformed from -Log10 (*P*-value). ***Abbreviation:*** Treg: regulatory T cell.

Figure 5. The heterogeneity of tumor associated neutrophils in ADC. A. UMAP plots showing the distribution of neutrophils in 15 samples (left), original clustering (middle) the re-clustering (right) into 3 sub-clusters according to gene markers of tumor-associated neutrophils (TANs). **B.** Dot heatmap showing the top 5 DEGs in each sub-cluster of TANs. **C.** UMAP plots for annotation of each sub-type of TANs with published marker genes presented: pro-tumor TANs, anti-tumor TANs and TANs with isg. **D.** UMAP and histogram plots to compare the differences of distribution and proportion of each sub-types of TANs between different histological types. **E.** GOBP analyses of signaling pathways that are more active in ADC than SCC, in terms of the pro-tumor TANs cluster. The histogram data are transformed from -Log_{10} (*P*-value). **F.** Kaplan-Meier curve showing the overall survival rate of CC patients stratified by the top 90 genes-scaled signature of pro-TANs.

Figure 6. Phenotype diversity of plasma/B cells in ADC. A. UMAP plots showing the distribution of plasma/B cells in 15 samples (left) and the re-clustering into 6 clusters (right) according to ectopic expressions of genes. **B.** Plot heatmap showing the annotation of each sub-cluster with top 5 DEGs. **C.** UMAP plots demonstrating

the most specific genes as the marker for each sub-cluster. **D.** UMAP and histogram plots to compare the differences of distribution and proportion of each plasma/B cell sub-cluster between different histological types. **E.** GOBP analysis of immunity-related signaling pathways that are more active in ADC, in terms of Plasma/B_01_IGHA2 sub-cluster. The histogram data are transformed from -Log_{10} (*P*-value). **F.** Kaplan-Meier curve showing the overall survival rate of CC patients stratified by the top 50 genes-scaled signature of Plasma/B_01_IGHA2.

Figure 7. The cellular interaction modules of sub-clusters of T cells, neutrophils and tumor epithelial cells. A. Circle plots showing the interacting networks between epithelial cell sub-clusters and T cell sub-clusters via the pathway of ALCAM, by comparing ADC and SCC. **B.** Circle plots simplified from **A** to show the interactions among target cell clusters via ALCAM pathway. **C.** Circle plots showing the interacting networks between epithelial cell sub-clusters and T cell sub-clusters via the pathway of MHC-II, by comparing ADC and SCC. **D.** Circle plots simplified from **C** to show the interactions among target cell clusters via MHC-II pathway. From **A** to **D**, The direction of each arrow shows the regulation from outputting cells to incoming cells. The width of the each line shows the predicted weight and strength of regulation. **E.** Bubble plot showing the probability of ligand-to-receptor combination of each pathway between two different target sub-clusters of cells, by comparing ADC with SCC. **F.** Circle plots showing Tregs regulate epithelial cells via the TGF-β pathway, which is solely activated in ADC. **G.** Bubble plot showing the probability of ligand-to-receptor combination of TGF-β pathway between Tregs and epithelial cells, by comparing ADC with SCC. The pathways of ADGRE5, CD46, GZMA and NAMPT are used as negative controls**. H.** Dual IF staining confirming that in $SLC26A3^{high}$ regions of CC tissues, more $FOXP3^{+}$ cells are recruited than in $SLC26A3^{low}$ regions (left). The numbers of recruited $FOXP3^{+}$ cell are quantified using histogram plot (right). Three individual samples with ROI were calculated and

P<0.01 were marked with **, showing significant difference. **I.** Multiplexed IF staining confirming the interaction between CD6 (on $FOXP3^+$ cells) and ALCAM (on $SLC26A3^+$ epithelial cells) in the ALCAM pathway. **J.** Multiplexed IF staining showing that the recruitment of FOXP3+ cells towards SLC26A3+ cells might induce EMT (marked with E-cadherin) and increase the stemness (marked with ALDH1A1) of tumor cells, via TGF-β pathway.

Tables

Table 1. The association between post-surgical upstaging and clinical characteristics in patient cohort 1 (from Xiangya hospital)

Characteristics	Cases number	Upstaging after surgery		χ^2	*P* value
		Yes	No		
Total	215				
Histological types	209				
ADC	55	8 (14.55%)	47 (85.45%)	0.955	0.328
SCC	154	15 (9.74%)	139 (90.26%)		
HPV status	196				
HPV+	181	18 (9.94%)	163 (90.06%)	3.887	0.049*
HPV-	15	4 (26.67%)	11 (73.33%)		
ADC with HPV status	50				
HPV+	40	4 (10.00%)	36 (90.00%)	5.357	0.021*
HPV-	10	4 (40.00%)	6 (60.00%)		
SCC with HPV status	143				
HPV+	138	13 (9.42%)	125 (90.58%)	0.518	0.472
HPV-	5	0 (0.00%)	5 (100%)		

***** $P < 0.05$ was considered as significantly different. $P < 0.01$ was presented as ******.
In each comparison panel, patients with insufficient data were excluded from analysis. The total number is 215, among which 6 cases are specific histological types (3 are neuroendocrine carcinoma (Neuro); 2 are adenosquamous carcinoma; 1 is malignant melanoma) and has been excluded for comparison between ADC and SCC. Because the HPV status information is unclear in 16 cases, a total number of 196 cases have been used for comparison between different HPV statuses. As for sub-classification between different HPV status under different histological types, 3 Neuro cases have been excluded.

Table 2. The association between post-surgical upstaging and clinical

characteristics in patient cohort 2 (from Hunan cancer hospital)

Characteristics	Cases number	Upstaging after surgery		χ^2	*P* value
		Yes	No		
Total	1398				
Histological types	1336				
ADC	190	40 (21.05%)	150 (78.95%)	4.911	0.027 *
SCC	1146	169 (14.75%)	977 (85.25%)		
HPV status	1166				
HPV+	1031	131 (12.71%)	900 (87.29%)	66.616	<0.001**
HPV-	135	54 (40.00%)	81 (60.00%)		
ADC with HPV status	162				
HPV+	131	18 (13.74%)	113 (86.26%)	24.999	<0.001**
HPV-	31	17 (54.84%)	14 (45.16%)		
SCC with HPV status	958				
HPV+	864	109 (12.62%)	755 (87.38%)	40.229	<0.001**
HPV-	94	35 (37.23%)	59 (62.77%)		
Neuro with HPV status	27				
HPV+	21	3 (14.29%)	18 (85.71%)	0.964	0.326
HPV-	6	0 (0.00%)	6 (100.00%)		
ADSCC with HPV status	14				
HPV+	12	1 (8.33%)	11 (91.67%)	2.431	0.119
HPV-	2	1 (50.00%)	1 (50.00%)		

***** $P < 0.05$ was considered as significantly different. $P < 0.01$ was presented as ******. Neuro is short for neuroendocrine carcinoma；ADSCC is short for adenosquamous carcinoma of cervix.

In each comparison panel, patients with insufficient data were excluded from analysis. The total number is 1398 and 62 cases have been excluded for comparison between ADC and SCC, due to special pathological types (Carcinosarcoma: 1; Melanoma: 1; Neuroendocrine carcinoma: 38; Basaloma: 1; Adenosquamous carcinoma: 18; Malignant peripheral nerve sheath tumor: 1; Fibroblastic sarcoma: 1; Adenosarcoma: 1). Because the HPV status information is unclear in 232 cases, a total number of 1166 cases has been used for comparison between different HPV status. As for sub-classification between two HPV statuses under different histological types, the excluded case numbers for each group are as follows due to unknown HPV status: 28 in ADC; 188 in SCC; 11 in Neuro; 4 in ADSCC (**Supplementary Fig. 3F**).

Table 3. The association between clinical characteristics and SLC26A3 protein

expression via IHC tested on post-surgical samples

Characteristics	Cases number	SLC26A3 expression		χ^2	*P* value
		High	Low		
Total	56				
Age	56				
⩾ 50	28	8 (28.57%)	20 (71.43%)	0.717	0.397
＜ 50	28	11 (39.29%)	17 (60.71%)		
Histological grading	51				
G1，G1-2	20	5 (25.00%)	15 (75.00%)	1.527	0.217
G2，G2-3，G3	31	13 (41.94%)	18 (50.06%)		
FIGO stages	56				
I-II (LN-M -)	47	12 (25.53%)	35 (74.47%)	9.198	**0.002****
IIICp (LN-M +)	9	7 (77.78%)	2 (22.22%)		
HPV status	53				
HPV+	44	13 (29.55%)	31 (70.45%)	2.254	0.133
HPV-	9	5 (55.56%)	4 (44.44%)		

***** $P < 0.05$ was considered as significantly different. $P < 0.01$ was presented as ******.

Table 4. The association between clinical characteristics and SLC26A3 protein

expression via IHC tested on biopsy small specimens

Characteristics	Cases number	SLC26A3 expression		χ^2	*P* value
		High	Low		
Total	43				
Age					
⩾ 50	16	3 (18.75%)	13 (81.25%)	4.605	0.032
＜ 50	27	14 (51.85%)	13 (48.15%)		
Histological grading					
G1，G1-2	9	4 (44.44%)	5 (55.56%)	0.115	0.735
G2，G2-3，G3	34	13 (38.24%)	21 (61.76%)		
FIGO stages					
I-II (consistent staging)	29	7 (24.14%)	22 (75.86%)	8.833	**0.003 ***
IIICp (upstaging)	14	10 (71.43%)	4 (28.57%)		
HPV status					
HPV+	32	10 (31.25%)	22 (68.75%)	3.592	0.058
HPV-	11	7 (63.64%)	4 (36.36%)		

***** $P < 0.05$ was considered as significantly different. $P < 0.01$ was presented as ******.

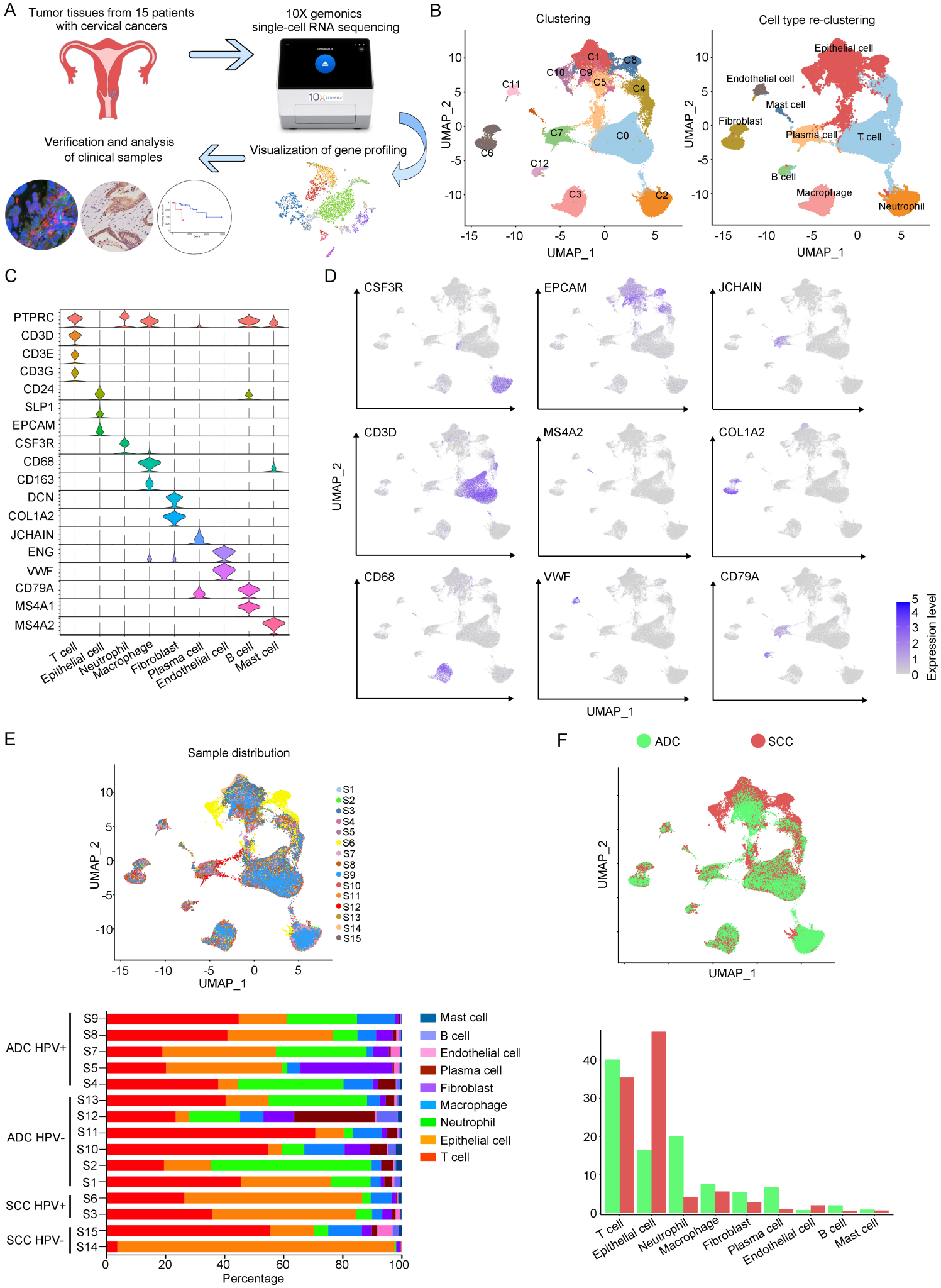
A
Tumor tissues from 15 patients with cervical cancers
10X gemonics single-cell RNA sequencing
Visualization of gene profiling
Verification and analysis of clinical samples
B
Clustering
Cell type re-clustering
UMAP_1
UMAP_2
C0
C1
C2
C3
C4
C5
C6
C7
C8
C9
C10
C11
C12
Epithelial cell
Endothelial cell
Mast cell
Fibroblast
Plasma cell
T cell
B cell
Macrophage
Neutrophil
C
PTPRC
CD3D
CD3E
CD3G
CD24
SLP1
EPCAM
CSF3R
CD68
CD163
DCN
COL1A2
JCHAIN
ENG
VWF
CD79A
MS4A1
MS4A2
T cell
Epithelial cell
Neutrophil
Macrophage
Fibroblast
Plasma cell
Endothelial cell
B cell
Mast cell
D
CSF3R
EPCAM
JCHAIN
CD3D
MS4A2
COL1A2
CD68
VWF
CD79A
UMAP_1
UMAP_2
Expression level
E
Sample distribution
S1
S2
S3
S4
S5
S6
S7
S8
S9
S10
S11
S12
S13
S14
S15
F
ADC
SCC
ADC HPV+
ADC HPV-
SCC HPV+
SCC HPV-
Mast cell
B cell
Endothelial cell
Plasma cell
Fibroblast
Macrophage
Neutrophil
Epithelial cell
T cell
Percentage

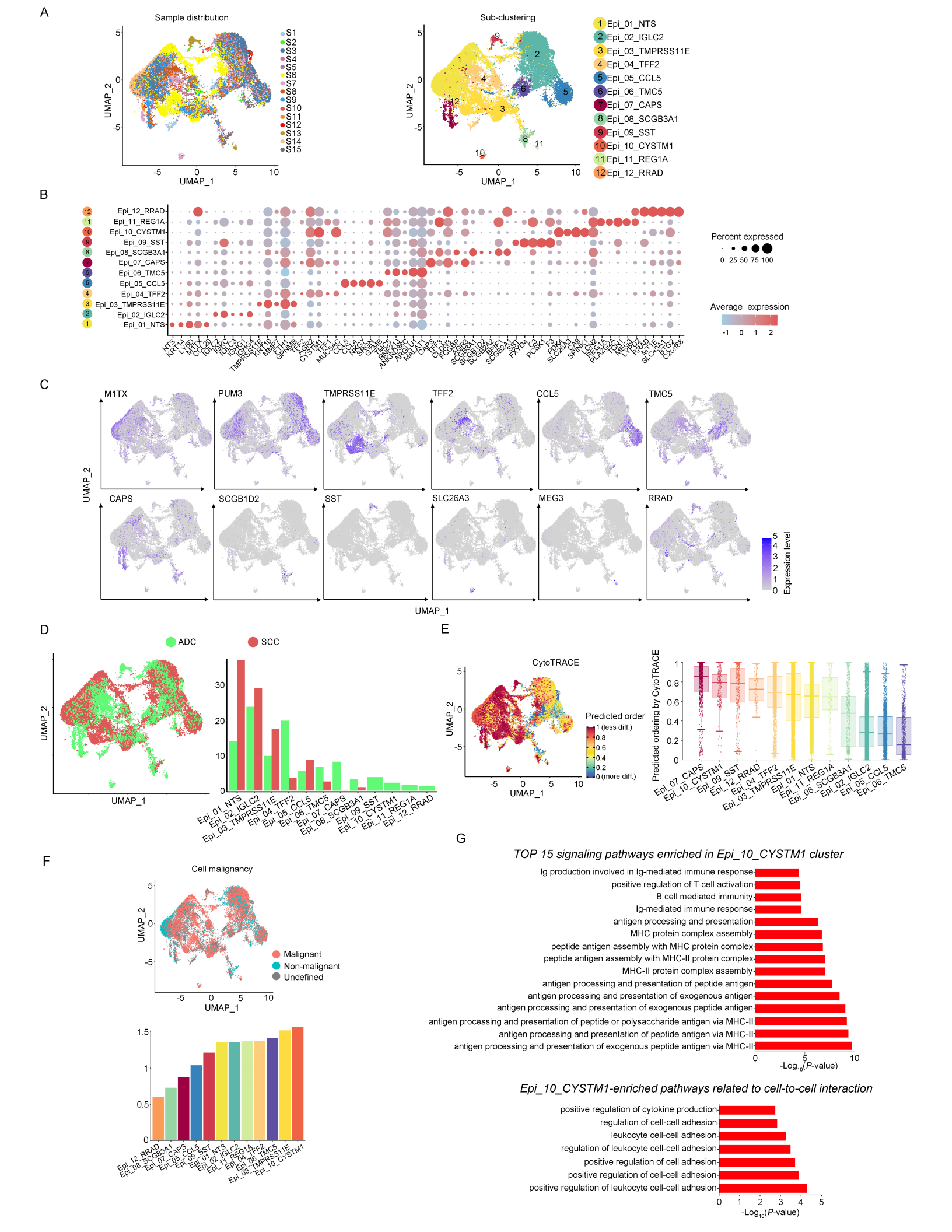
A
Sample distribution
S1
S2
S3
S4
S5
S6
S7
S8
S9
S10
S11
S12
S13
S14
S15
UMAP_1
UMAP_2
Sub-clustering
1 Epi_01_NTS
2 Epi_02_IGLC2
3 Epi_03_TMPRSS11E
4 Epi_04_TFF2
5 Epi_05_CCL5
6 Epi_06_TMC5
7 Epi_07_CAPS
8 Epi_08_SCGB3A1
9 Epi_09_SST
10 Epi_10_CYSTM1
11 Epi_11_REG1A
12 Epi_12_RRAD
B
Percent expressed
0 25 50 75 100
Average expression
-1 0 1 2
C
M1TX
PUM3
TMPRSS11E
TFF2
CCL5
TMC5
CAPS
SCGB1D2
SST
SLC26A3
MEG3
RRAD
Expression level
D
ADC
SCC
E
CytoTRACE
Predicted order
1 (less diff.)
0 (more diff.)
Predicted ordering by CytoTRACE
F
Cell malignancy
Malignant
Non-malignant
Undefined
G
TOP 15 signaling pathways enriched in Epi_10_CYSTM1 cluster
Ig production involved in Ig-mediated immune response
positive regulation of T cell activation
B cell mediated immunity
Ig-mediated immune response
antigen processing and presentation
MHC protein complex assembly
peptide antigen assembly with MHC protein complex
peptide antigen assembly with MHC-II protein complex
MHC-II protein complex assembly
antigen processing and presentation of peptide antigen
antigen processing and presentation of exogenous antigen
antigen processing and presentation of exogenous peptide antigen
antigen processing and presentation of peptide or polysaccharide antigen via MHC-II
antigen processing and presentation of peptide antigen via MHC-II
antigen processing and presentation of exogenous peptide antigen via MHC-II
-Log10(P-value)
Epi_10_CYSTM1-enriched pathways related to cell-to-cell interaction
positive regulation of cytokine production
regulation of cell-cell adhesion
leukocyte cell-cell adhesion
regulation of leukocyte cell-cell adhesion
positive regulation of cell adhesion
positive regulation of cell-cell adhesion
positive regulation of leukocyte cell-cell adhesion
-Log10(P-value)

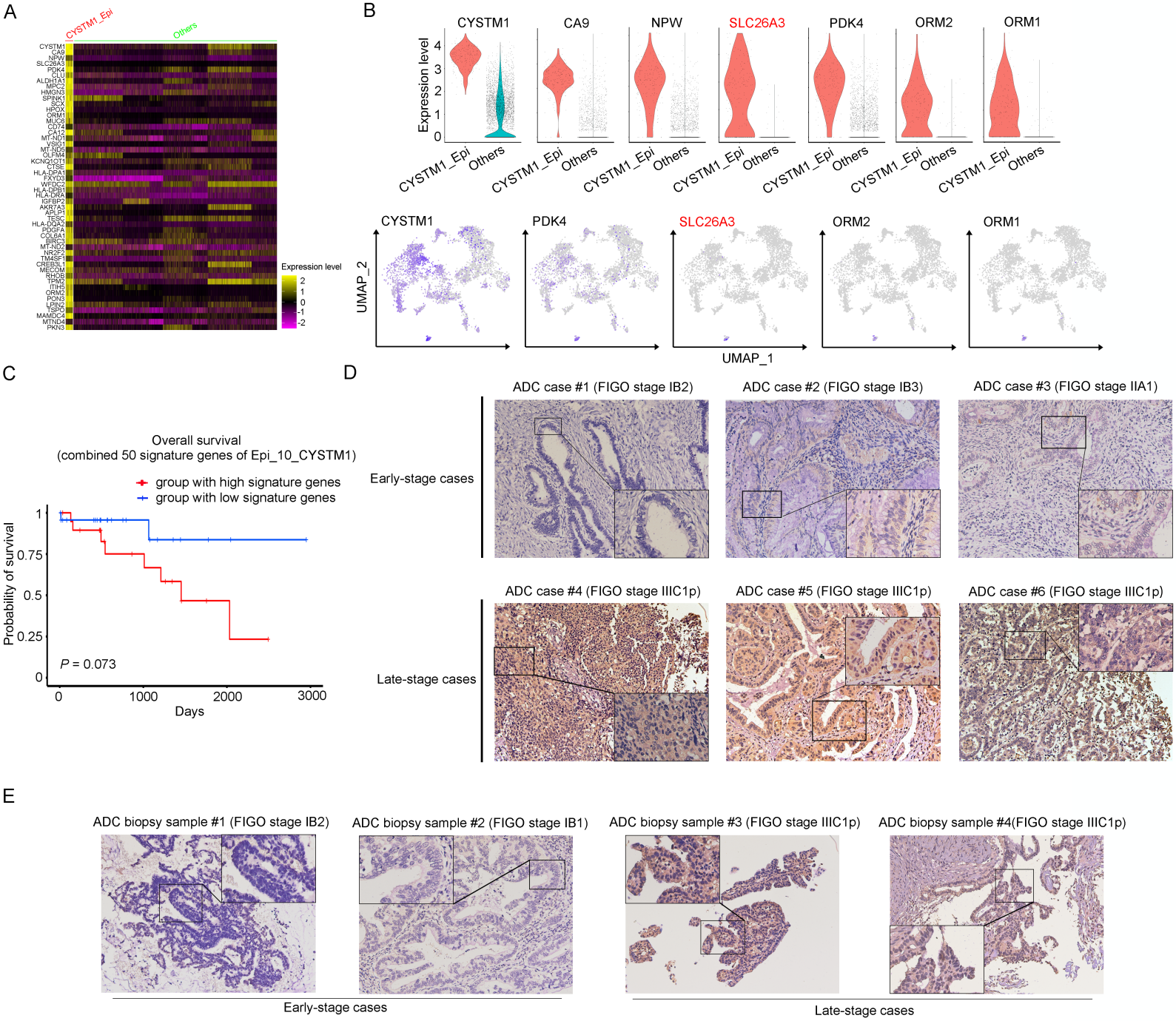
A
CYSTM1_Epi
Others
Expression level
B
CYSTM1
CA9
NPW
SLC26A3
PDK4
ORM2
ORM1
Expression level
CYSTM1_Epi
Others
UMAP_2
UMAP_1
C
Overall survival
(combined 50 signature genes of Epi_10_CYSTM1)
group with high signature genes
group with low signature genes
Probability of survival
P = 0.073
Days
D
ADC case #1 (FIGO stage IB2)
ADC case #2 (FIGO stage IB3)
ADC case #3 (FIGO stage IIA1)
Early-stage cases
ADC case #4 (FIGO stage IIIC1p)
ADC case #5 (FIGO stage IIIC1p)
ADC case #6 (FIGO stage IIIC1p)
Late-stage cases
E
ADC biopsy sample #1 (FIGO stage IB2)
ADC biopsy sample #2 (FIGO stage IB1)
ADC biopsy sample #3 (FIGO stage IIIC1p)
ADC biopsy sample #4(FIGO stage IIIC1p)
Early-stage cases
Late-stage cases

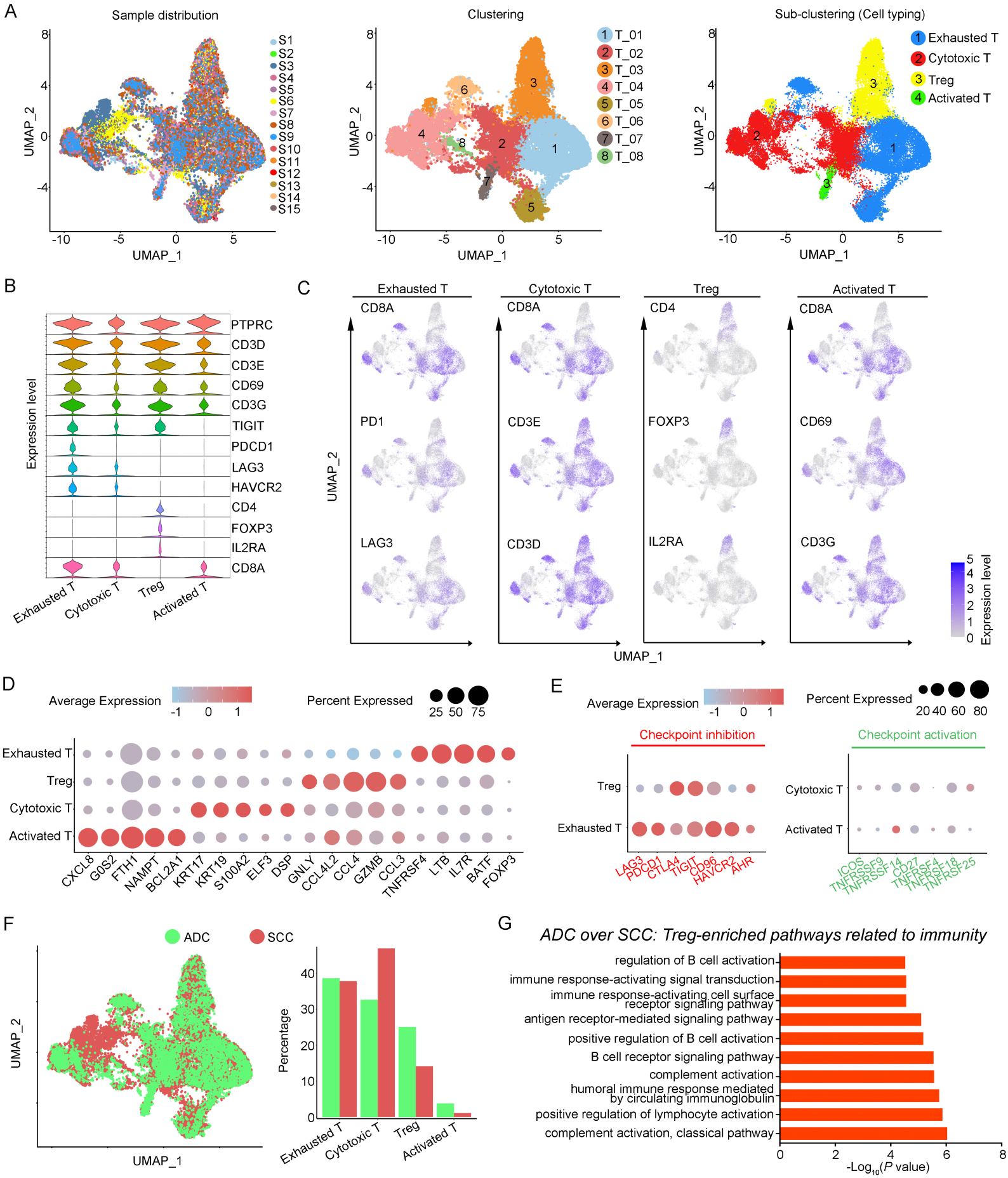
A
Sample distribution
Clustering
Sub-clustering (Cell typing)
UMAP_1
UMAP_2
S1
S2
S3
S4
S5
S6
S7
S8
S9
S10
S11
S12
S13
S14
S15
T_01
T_02
T_03
T_04
T_05
T_06
T_07
T_08
Exhausted T
Cytotoxic T
Treg
Activated T
B
Expression level
PTPRC
CD3D
CD3E
CD69
CD3G
TIGIT
PDCD1
LAG3
HAVCR2
CD4
FOXP3
IL2RA
CD8A
C
CD8A
PD1
LAG3
CD3E
CD3D
CD4
FOXP3
IL2RA
CD69
CD3G
D
Average Expression
Percent Expressed
CXCL8
G0S2
FTH1
NAMPT
BCL2A1
KRT17
KRT19
S100A2
ELF3
DSP
GNLY
CCL4L2
CCL4
GZMB
CCL3
TNFRSF4
LTB
IL7R
BATF
FOXP3
E
Checkpoint inhibition
Checkpoint activation
LAG3
PDCD1
CTLA4
TIGIT
CD96
HAVCR2
AHR
ICOS
TNFRSF9
TNFRSF14
CD27
TNFRSF4
TNFRSF18
TNFRSF25
F
ADC
SCC
Percentage
G
ADC over SCC: Treg-enriched pathways related to immunity
regulation of B cell activation
immune response-activating signal transduction
immune response-activating cell surface receptor signaling pathway
antigen receptor-mediated signaling pathway
positive regulation of B cell activation
B cell receptor signaling pathway
complement activation
humoral immune response mediated by circulating immunoglobulin
positive regulation of lymphocyte activation
complement activation, classical pathway
-Log10(P value)

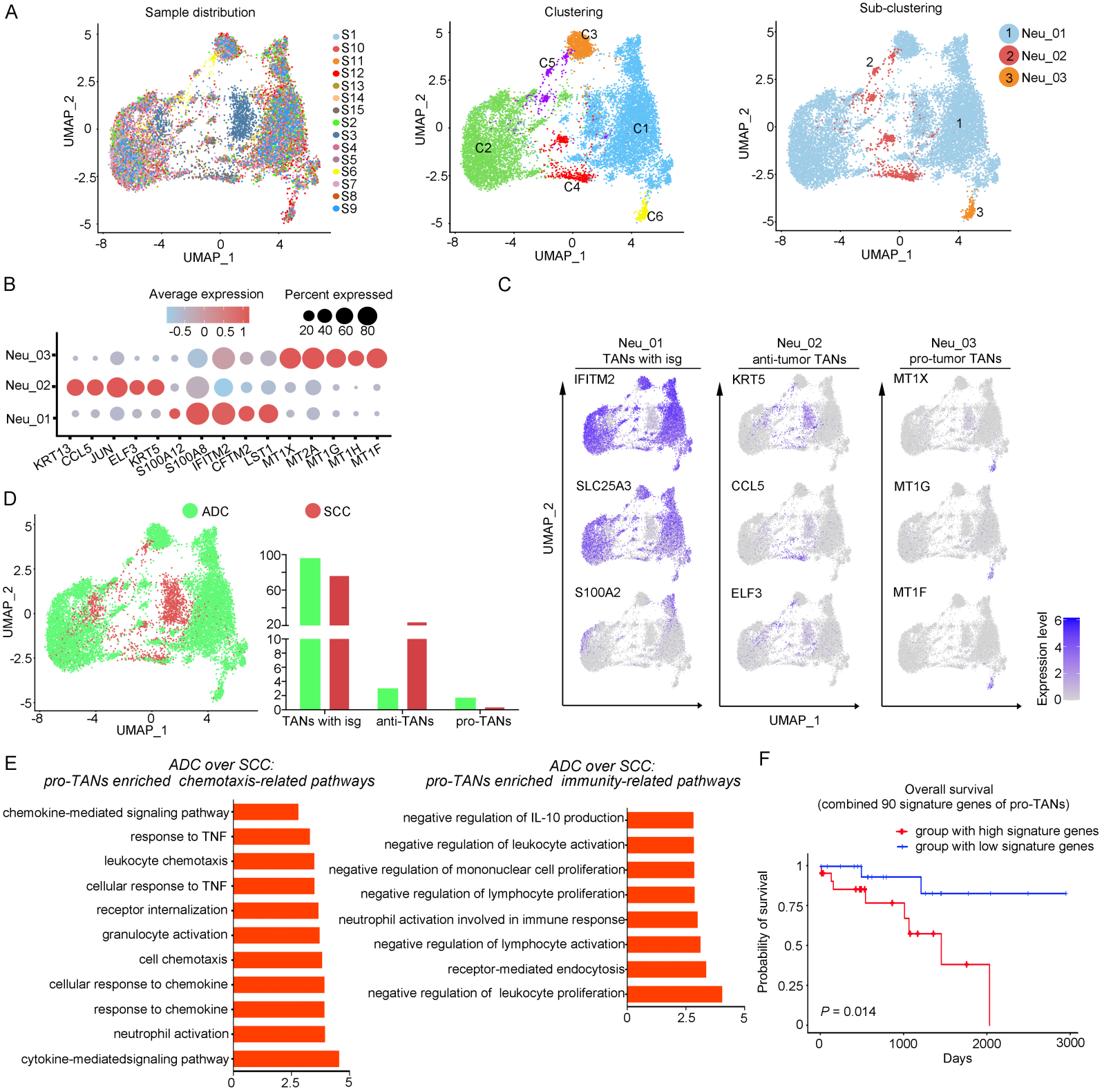
A
Sample distribution
Clustering
Sub-clustering
UMAP_1
UMAP_2
S1
S10
S11
S12
S13
S14
S15
S2
S3
S4
S5
S6
S7
S8
S9
C1
C2
C3
C4
C5
C6
1 Neu_01
2 Neu_02
3 Neu_03
B
Average expression
Percent expressed
Neu_03
Neu_02
Neu_01
KRT13
CCL5
JUN
ELF3
KRT5
S100A12
S100A8
IFITM2
CFTM2
LST1
MT1X
MT2A
MT1G
MT1H
MT1F
C
Neu_01
TANs with isg
Neu_02
anti-tumor TANs
Neu_03
pro-tumor TANs
IFITM2
SLC25A3
S100A2
KRT5
CCL5
ELF3
MT1X
MT1G
MT1F
Expression level
D
ADC
SCC
TANs with isg
anti-TANs
pro-TANs
E
ADC over SCC:
pro-TANs enriched chemotaxis-related pathways
chemokine-mediated signaling pathway
response to TNF
leukocyte chemotaxis
cellular response to TNF
receptor internalization
granulocyte activation
cell chemotaxis
cellular response to chemokine
response to chemokine
neutrophil activation
cytokine-mediatedsignaling pathway
ADC over SCC:
pro-TANs enriched immunity-related pathways
negative regulation of IL-10 production
negative regulation of leukocyte activation
negative regulation of mononuclear cell proliferation
negative regulation of lymphocyte proliferation
neutrophil activation involved in immune response
negative regulation of lymphocyte activation
receptor-mediated endocytosis
negative regulation of leukocyte proliferation
F
Overall survival
(combined 90 signature genes of pro-TANs)
group with high signature genes
group with low signature genes
Probability of survival
Days
P = 0.014

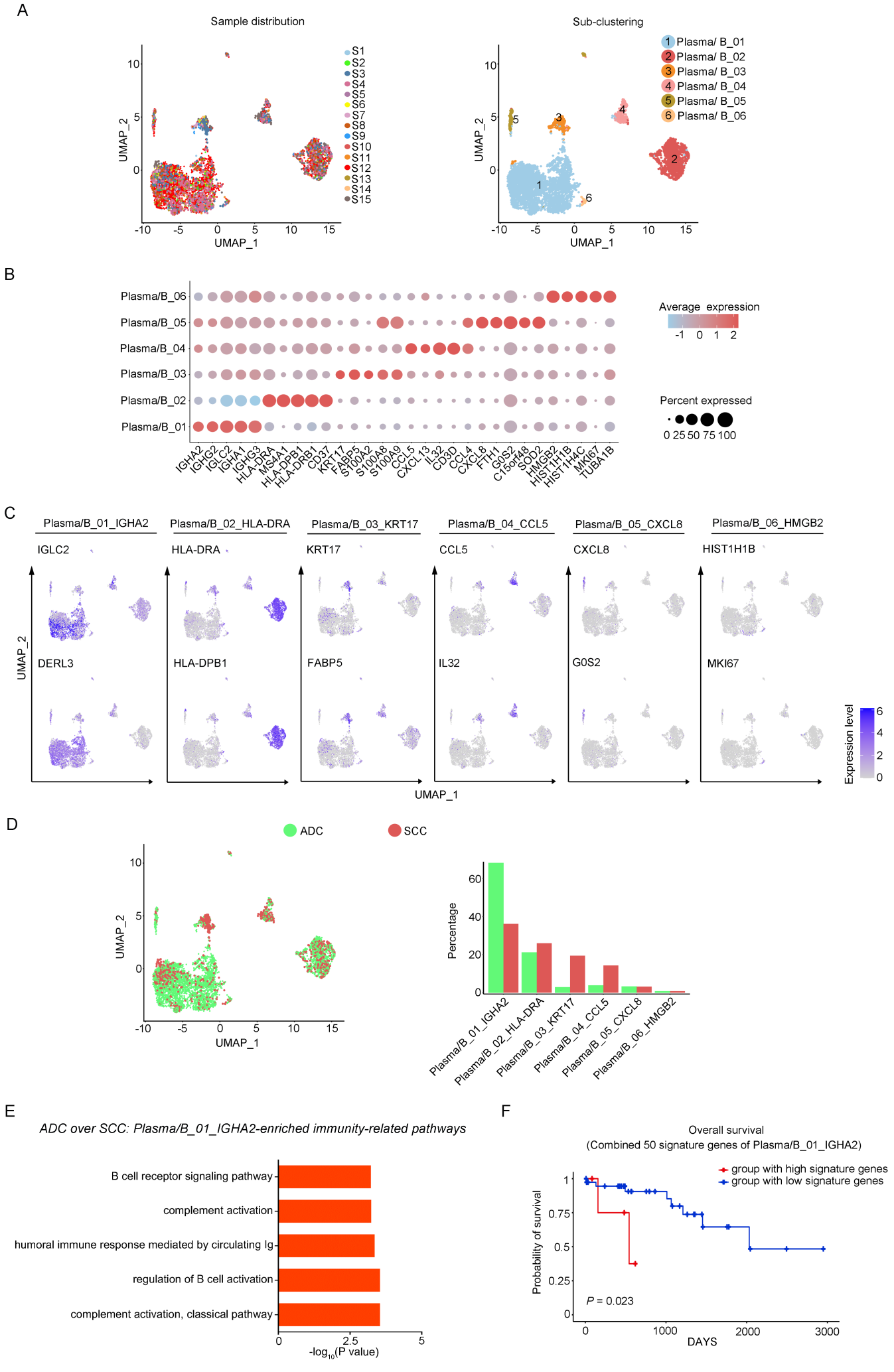
A
Sample distribution
Sub-clustering
UMAP_1
UMAP_2
S1
S2
S3
S4
S5
S6
S7
S8
S9
S10
S11
S12
S13
S14
S15
1 Plasma/ B_01
2 Plasma/ B_02
3 Plasma/ B_03
4 Plasma/ B_04
5 Plasma/ B_05
6 Plasma/ B_06
B
Plasma/B_06
Plasma/B_05
Plasma/B_04
Plasma/B_03
Plasma/B_02
Plasma/B_01
IGHA2
IGHG2
IGLC2
IGHA1
IGHG3
HLA-DRA
MS4A1
HLA-DPB1
HLA-DRB1
CD37
KRT17
FABP5
S100A2
S100A8
S100A9
CCL5
CXCL13
IL32
CD3D
CCL4
CXCL8
FTH1
G0S2
C15orf48
SOD2
HMGB2
HIST1H1B
HIST1H4C
MKI67
TUBA1B
Average expression
-1 0 1 2
Percent expressed
0 25 50 75 100
C
Plasma/B_01_IGHA2
Plasma/B_02_HLA-DRA
Plasma/B_03_KRT17
Plasma/B_04_CCL5
Plasma/B_05_CXCL8
Plasma/B_06_HMGB2
IGLC2
HLA-DRA
KRT17
CCL5
CXCL8
HIST1H1B
DERL3
HLA-DPB1
FABP5
IL32
G0S2
MKI67
Expression level
D
ADC
SCC
Percentage
E
ADC over SCC: Plasma/B_01_IGHA2-enriched immunity-related pathways
B cell receptor signaling pathway
complement activation
humoral immune response mediated by circulating Ig
regulation of B cell activation
complement activation, classical pathway
-log10(P value)
F
Overall survival
(Combined 50 signature genes of Plasma/B_01_IGHA2)
group with high signature genes
group with low signature genes
Probability of survival
P = 0.023
DAYS

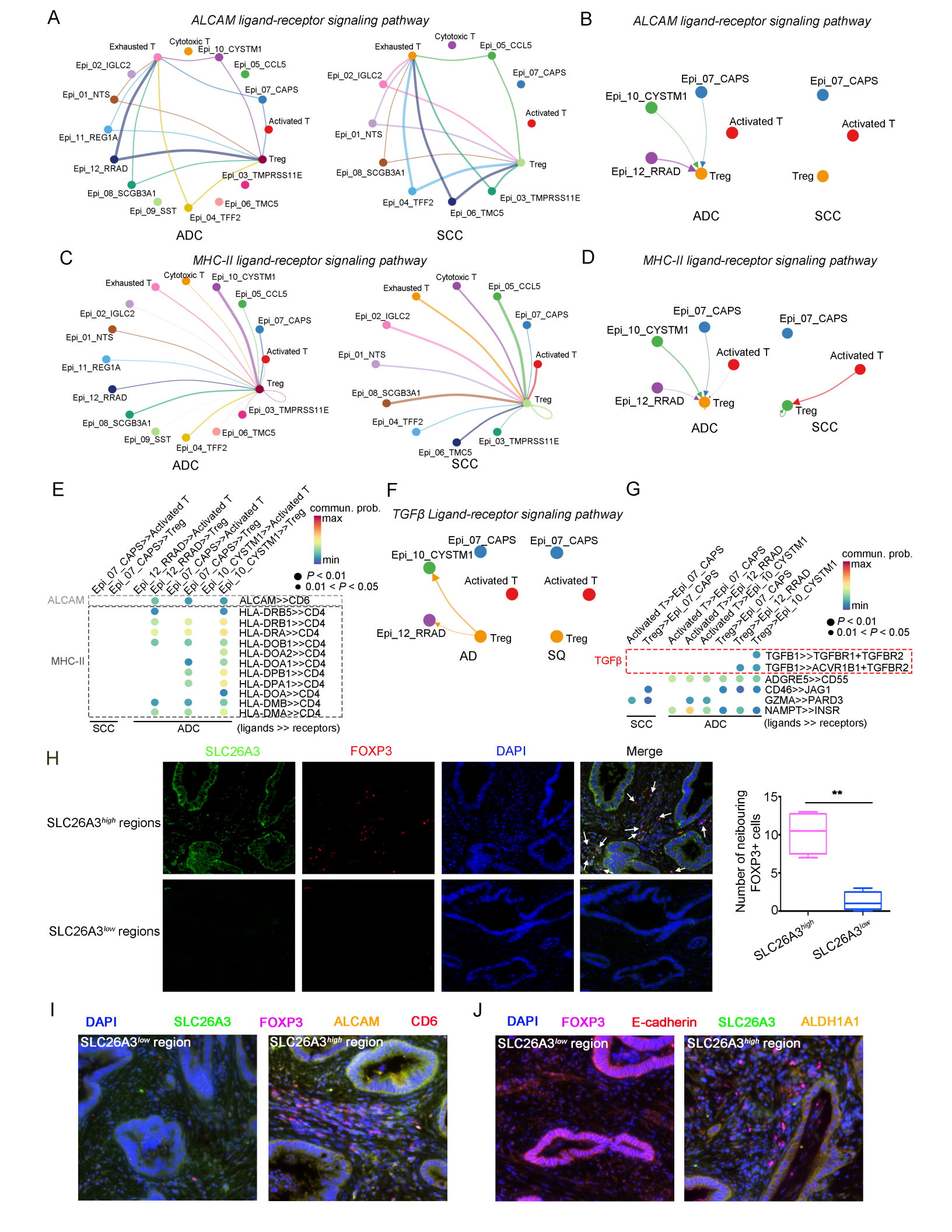
A
ALCAM ligand-receptor signaling pathway
Exhausted T
Cytotoxic T
Epi_10_CYSTM1
Epi_02_IGLC2
Epi_05_CCL5
Epi_01_NTS
Epi_07_CAPS
Activated T
Epi_11_REG1A
Treg
Epi_12_RRAD
Epi_03_TMPRSS11E
Epi_08_SCGB3A1
Epi_06_TMC5
Epi_09_SST
Epi_04_TFF2
ADC
SCC
B
ALCAM ligand-receptor signaling pathway
C
MHC-II ligand-receptor signaling pathway
D
MHC-II ligand-receptor signaling pathway
E
commun. prob.
max
min
P < 0.01
0.01 < P < 0.05
Epi_07_CAPS>>Activated T
Epi_07_CAPS>>Treg
Epi_12_RRAD>>Activated T
Epi_12_RRAD>>Treg
Epi_10_CYSTM1>>Activated T
Epi_10_CYSTM1>>Treg
ALCAM
ALCAM>>CD6
MHC-II
HLA-DRB5>>CD4
HLA-DRB1>>CD4
HLA-DRA>>CD4
HLA-DOB1>>CD4
HLA-DOA2>>CD4
HLA-DOA1>>CD4
HLA-DPB1>>CD4
HLA-DPA1>>CD4
HLA-DOA>>CD4
HLA-DMB>>CD4
HLA-DMA>>CD4
SCC
ADC
(ligands >> receptors)
F
TGFβ Ligand-receptor signaling pathway
Epi_07_CAPS
Epi_10_CYSTM1
Activated T
Epi_12_RRAD
Treg
AD
SQ
G
Activated T>>Epi_07_CAPS
Treg>>Epi_07_CAPS
Activated T>>Epi_12_RRAD
Treg>>Epi_12_RRAD
Activated T>>Epi_10_CYSTM1
Treg>>Epi_10_CYSTM1
TGFβ
TGFB1>>TGFBR1+TGFBR2
TGFB1>>ACVR1B1+TGFBR2
ADGRE5>>CD55
CD46>>JAG1
GZMA>>PARD3
NAMPT>>INSR
SCC
ADC
(ligands >> receptors)
H
SLC26A3
FOXP3
DAPI
Merge
SLC26A3high regions
SLC26A3low regions
Number of neibouring FOXP3+ cells
15
10
5
0
**
SLC26A3high
SLC26A3low
I
DAPI
SLC26A3
FOXP3
ALCAM
CD6
SLC26A3low region
SLC26A3high region
J
DAPI
FOXP3
E-cadherin
SLC26A3
ALDH1A1
SLC26A3low region
SLC26A3high region